Article

Basis of narrow-spectrum activity of fidaxomicin on *Clostridioides difficile*

https://doi.org/10.1038/s41586-022-04545-z

Received: 22 August 2021

Accepted: 10 February 2022

Published online: 6 April 2022

Check for updates

Xinyun Cao[1,4], Hande Boyaci[2,4], James Chen[2], Yu Bao[1], Robert Landick[1,3] ✉ & Elizabeth A. Campbell[2] ✉

Fidaxomicin (Fdx) is widely used to treat *Clostridioides difficile* (*Cdiff*) infections, but the molecular basis of its narrow-spectrum activity in the human gut microbiome remains unknown. *Cdiff* infections are a leading cause of nosocomial deaths[1]. Fidaxomicin, which inhibits RNA polymerase, targets *Cdiff* with minimal effects on gut commensals, reducing recurrence of *Cdiff* infection[2,3]. Here we present the cryo-electron microscopy structure of *Cdiff* RNA polymerase in complex with fidaxomicin and identify a crucial fidaxomicin-binding determinant of *Cdiff* RNA polymerase that is absent in most gut microbiota such as Proteobacteria and Bacteroidetes. By combining structural, biochemical, genetic and bioinformatic analyses, we establish that a single residue in *Cdiff* RNA polymerase is a sensitizing element for fidaxomicin narrow-spectrum activity. Our results provide a blueprint for targeted drug design against an important human pathogen.

Cdiff is a Gram-positive, spore-forming, and toxin-producing intestinal bacterium that infects the human gut and causes lethal diarrhea. Numbers of infections caused by highly pathogenic variants are increasing, leading to *Cdiff* being designated an 'urgent threat' by the US Centers for Disease Control and Prevention[1]. Broad-spectrum antibiotics such as vancomycin and metronidazole are used to treat *Cdiff* infections, but these antibiotics decimate the normal gut microbiome, paradoxically priming the gastrointestinal tract to become more prone to recurrences of *Cdiff* infection[2,3] (Fig. 1a). In 2011, the macrocyclic antibiotic fidaxomicin (Fdx) (Fig. 1b) became available to treat *Cdiff* infection. Fdx selectively targets *Cdiff* but does not effectively kill crucial gut commensals such as Bacteroidetes[4], which are abundant in the human gut microbiome and protect against *Cdiff* colonization[5,6]. Fdx targets the multisubunit bacterial RNA polymerase (RNAP) (subunit composition $\alpha_2\beta\beta'\omega$), which transcribes DNA to RNA in a complex and highly regulated process. However, no structure is available for Clostridial RNAP. Studies using *Mycobacterium tuberculosis* (*Mtb*) and *Escherichia coli* RNAPs show that Fdx functions by inhibiting initiation of transcription[7–10]. RNAP forms two mobile pincers that surround DNA[11,12] and Fdx inhibits initiation by jamming these pincers in an 'open' state, preventing one pincer—the clamp—from closing on the DNA. This doorstop-like jamming results in the enzyme being unable to both melt promoter DNA and secure the DNA in its active-site cleft. Although the general architecture of RNAP is similar in all organisms, differences in the primary subunit sequences, peripheral subunits or lineage-specific insertions that occur in bacterial RNAP[13] could explain Fdx sensitivity. For example, *Mtb* RNAP is much more sensitive to Fdx than *E. coli* RNAP[7], and the essential transcription factor RbpA sensitizes *Mtb* to Fdx even further[7]. The half-maximal inhibitory concentration (IC50) is 0.2 μM for *Mtb* RNAP with full-length RbpA, 7 μM for *Mtb* RNAP lacking the RbpA–Fdx contacts, and 53 μM for *E. coli* RNAP[7] (Supplementary Table 1). However, *Cdiff* lacks RbpA, leaving the molecular basis of *Cdiff* sensitivity to Fdx unresolved.

The pathogenicity and limited availability of genetic tools for *Cdiff* complicate using *Cdiff* directly for structural and mechanistic studies of RNAP, with a single report of endogenous *Cdiff* RNAP purification yielding small amounts of enzyme with suboptimal activity[14]. To enable studies of *Cdiff* RNAP, we created a recombinant system in *E. coli* that yields milligram quantities of *Cdiff* core RNAP (E) and also enables rapid mutagenesis (Methods and Supplementary Information). We also expressed the *Cdiff* housekeeping σ^A factor in *E. coli*, purified it, and combined it with core *Cdiff* RNAP to produce the holoenzyme ($E\sigma^A$). The purity, activity and yield of $E\sigma^A$ were suitable for structural and biochemical studies (Extended Data Fig. 1a–c).

To visualize the binding of Fdx to its clinical target, we used single particle cryo-electron microscopy (cryo-EM) to solve the structure of *Cdiff* $E\sigma^A$ in complex with Fdx. We obtained a cryo-EM map representing a single structural class comprising *Cdiff* $E\sigma^A$ and bound Fdx at 3.3 Å nominal resolution, with a local resolution of approximately 2.7–3 Å around the Fdx-binding pocket[15] (Fig. 1c, Extended Data Figs. 2, 3, Supplementary Table 2). The structure reveals key features of the *Cdiff* $E\sigma^A$ and provides the first view of a Clostridial $E\sigma^A$.

Cdiff RNAP contains a lineage-specific insert in the β lobe domain that resembles one found in RNAP from *Bacillus subtilis* (like *Cdiff*, a Firmicute), but distinct from the better-characterized inserts in *E. coli* RNAP[16–18]. The Firmicute β insert corresponds to βi5 identified by sequence analysis[13] and consists of two copies of the β–β′ module 2 (BBM2) protein fold whereas the β lobe insert in *E. coli* RNAP occurs at a different position and corresponds to βi4 (Extended Data Fig. 4). Our structure revealed that *Cdiff* βi5 (4–5 Å resolution; Extended Data Fig. 3) at a position similar to *B. subtilis* βi5[17] but the *Cdiff* insert is larger (121 amino acids versus 99 amino acids in *B. subtilis*) (Extended Data Fig. 4).

[1]Department of Biochemistry, University of Wisconsin–Madison, Madison, WI, United States. [2]Laboratory of Molecular Biophysics, The Rockefeller University, New York, NY, United States. [3]Department of Bacteriology, University of Wisconsin–Madison, Madison, WI, United States. [4]These authors contributed equally: Xinyun Cao, Hande Boyaci. ✉e-mail: rlandick@wisc.edu; campbee@rockefeller.edu

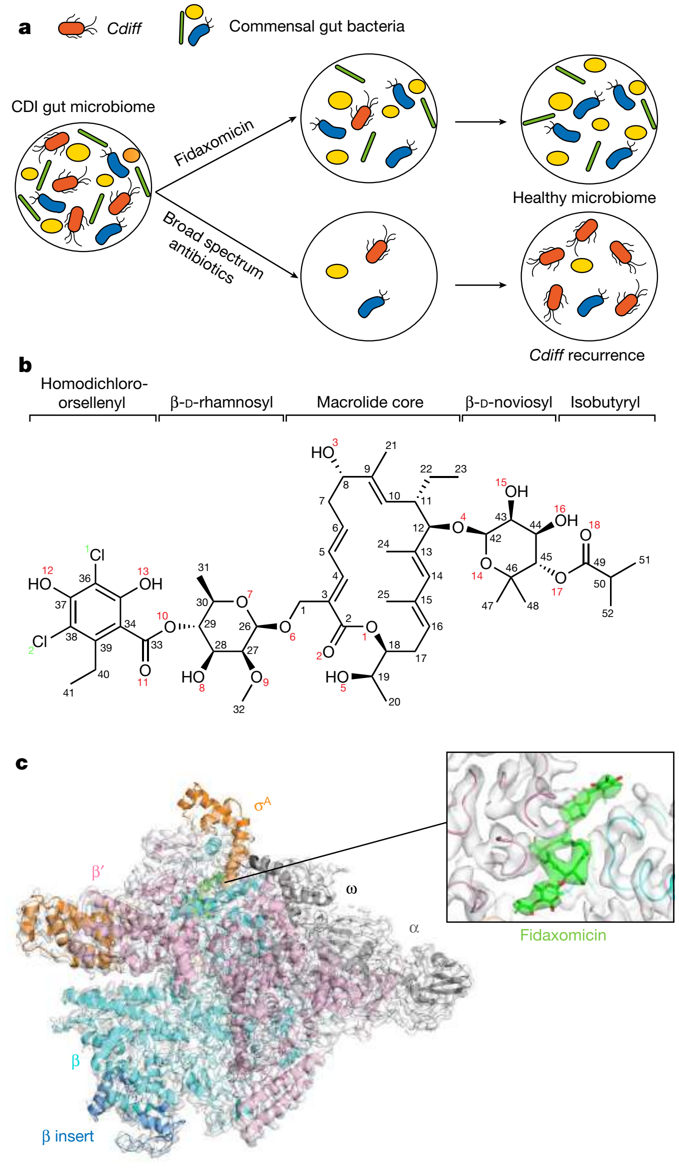

Fig. 1 | Fidaxomicin is a narrow-spectrum antimicrobial that inhibits RNAP. **a**, How fidaxomicin specifically targets *Cdiff* without affecting gut commensals and thus reduces recurrence (top circles). For patients with *Cdiff* infection treated with broad-spectrum antibiotics (bottom circles), the abundance of gut commensals drops simultaneously with *Cdiff*, resulting in high rates of *Cdiff* recurrence. **b**, Chemical structure of Fdx. **c**, Cryo-EM structure of *Cdiff* Eσ^A in complex with Fdx. The Eσ^A model is coloured by subunits, and the 3.26 Å cryo-EM map is represented as a white transparent surface. The cryo-EM density for Fdx is shown in the inset as a green transparent surface.

The function of the Firmicute βi5 is unknown and awaits further study but is unlikely to affect Fdx binding or activity, as it is located about 70 Å away.

Cdiff σ^A includes all conserved regions of σ, which were located in the *Cdiff* Eσ^A structure at locations similar to those seen for other bacterial housekeeping σ-factors[7,19,20] (Extended Data Fig. 5). Cryo-EM density was not visible for most of σ region 1 (residues 1–115 of the 150 residues in *Cdiff* region 1), as also seen with other bacterial holoenzymes characterized structurally[7,20,21]. *Cdiff* σ^A lacks the non-conserved region (NCR) insert between regions 1 and 2 that are found in some other bacteria, such as *E. coli*[16] (Extended Data Fig. 5).

As seen in other RNAPs[7,8,22], Fdx appears to stabilize the clamp pincer in an open state, but the *Cdiff* clamp is twisted slightly towards Fdx relative to the *Mtb* Eσ^A structure with Fdx (Fig. 2a). Opening and closing of the pincers are required for transcription initiation[11,22]. Fdx binds *Mtb* RNAP at a hinge between two RNAP pincers (the β′ clamp and β lobe pincers), thus physically jamming the hinge and locking RNAP in an open conformation that is unable to form a stable initiation complex[7,8]. Fdx occupies the same location in the *Cdiff* Eσ^A–Fdx structure, indicating that the hinge-jamming mechanism is widely conserved. However, the slight twisting of the *Cdiff* β′ clamp pincer relative to that observed in Fdx-bound *Mtb* RNAP (Fig. 2a) increases clamp–Fdx contacts.

Fdx contacts six key structural components of *Cdiff* RNAP: the β clamp, the β′ switch region 2 (SW2), β switch region 3 (SW3), β switch region 4 (SW4), β′ zinc-binding-domain (ZBD) and β′ lid (Figs. 2b, 3). We compared the Fdx-binding determinants in *Cdiff* RNAP to those previously determined in *Mtb* RNAP[7,8]. Most of the interactions between Fdx and RNAP were conserved between the two species (Extended Data Fig. 6a, Supplementary Table 3). In *Cdiff* RNAP (*Mtb* numbering in parentheses), Fdx formed direct hydrogen bonds or salt bridges with four residues β R1121 (K1101), β′ K84 (R84), β′ K86 (K86) and β′ R326 (R412) and two water-mediated hydrogen bonds with β′ D237 (E323) and σ H294 (Q434). (Fig. 2b, Extended Data Fig. 6a, Supplementary Table 3). Fdx binding is also stabilized by a cation–π interaction between the β′ R89 and the Fdx macrolide core C3–C5 double bond in both *Mtb* and *Cdiff* RNAPs. *Cdiff* RNAP residues known to confer Fdx resistance when mutated[23,24] (β V1143G, β V1143D, β V1143F, β′ D237Y and β Q1074K) were located within 5 Å of Fdx (Extended Data Fig. 6a).

Of note, β′ K84 in *Cdiff* RNAP forms a salt bridge with the oxygen on the phenolic group of Fdx (owing to the acidity of phenol), whereas the corresponding residue (β′ R84) in *Mtb* forms a cation–π interaction with the aromatic ring of the Fdx homodichloroorsellinic acid moiety (Fig. 2b). We propose that these coulombic interactions by β′ K84 (β′ R84) sensitize both RNAPs to tight Fdx binding (see comparison of individual residues in *Cdiff* and *Mtb* RNAPs that bind Fdx; Extended Data Fig. 6, Supplementary Table 3). *Mtb* RbpA, an essential transcriptional regulator in mycobacteria, lowers the IC50 of Fdx by a factor of 35 via Fdx contacts with two RbpA residues in the N-terminal region[7]. *Cdiff* RNAP lacks a RbpA homologue, but we observed four hydrophobic interactions between Fdx and *Cdiff* RNAP (with β T1073, β′ M319, β′ K314 and σ L283) and one water-mediated hydrogen bonding interaction with σ H294 that are not present with the corresponding *Mtb* RNAP residues (Fig. 2b, Extended Data Fig. 6, Supplementary Table 3). Some of these interactions (β′ M319 and β′ K314 in the clamp) with Fdx are created by the relatively increased rotation of the *Cdiff* RNAP clamp towards Fdx (Fig. 2a).

Gram-negative bacteria are more resistant to Fdx than Gram-positive bacteria[25–27]. This dichotomy could reflect differences in membrane and cell-wall morphology, differences in RNAPs, or both. To compare the activity of Fdx against *Cdiff* and *Mtb* RNAP, we performed abortive transcription assays using purified RNAPs and the native *Cdiff rrnC* ribosomal RNA promoter[14] (Fig. 2c). The IC50s of Fdx for *Cdiff* RNAP Eσ^A (approximately 0.2 μM) and *Mtb* Eσ^A including RbpA (approximately 0.3 μM) are similar, consistent with our structural observations (Fig. 2d, Extended Data Fig. 7). These IC50 values are two orders of magnitude lower than that for the *E. coli* σ^{70}-holoenzyme (Eσ^{70}) on the same DNA template (Fig. 2d, Extended Data Fig. 7), suggesting that the differences in RNAPs contribute to the differences in minimum inhibitory concentrations (MICs) between *Cdiff* (a Gram-positive) and Gram-negative bacteria. This observation suggests that the Fdx-binding residues identified in *Mtb* and *Cdiff* RNAPs can be used as a reference to predict Fdx potency in other bacterial species, including gut commensals[25].

We next used our *Mtb* and *Cdiff* RNAP–Fdx structures to predict the interactions responsible for the narrow spectrum activity of Fdx. Using sequence alignments of β′ and β from bacterial species with reported Fdx MICs[25,27] (Extended Data Fig. 8), we found that the Fdx-binding residues identified in *Mtb* and *Cdiff* RNAP are mostly conserved among these divergent bacteria, except for the aforementioned β′ K84 (β′ R84 in *Mtb*) and β′ S85 (β′ A85 in *Mtb*). β′ K84 and S85 are located in the ZBD. β′ K84 forms a salt bridge with the probably ionized Fdx O13

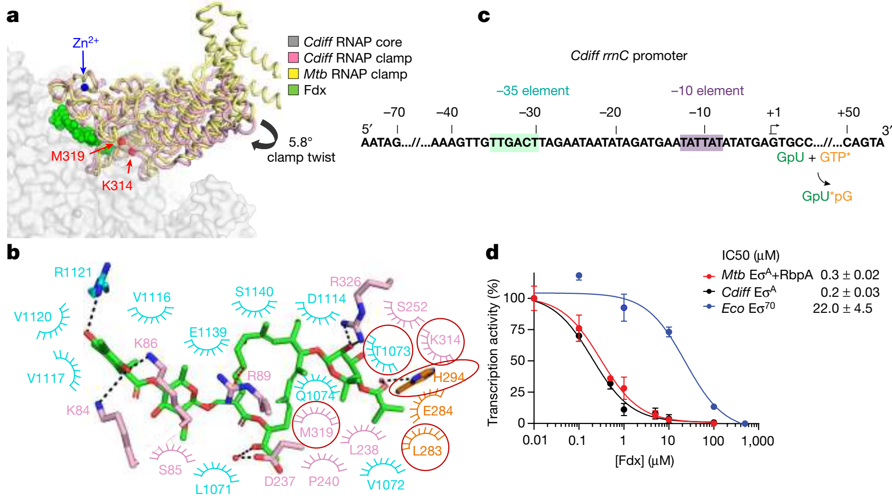

Fig. 2 | Fdx binding and inhibition of the *Cdiff* $E\sigma^{A}$. **a**, Differences in the clamp between *Cdiff* and *Mtb* RNAP. The *Cdiff* RNAP clamp (pink) is twisted 5.8° towards Fdx compared with the *Mtb* RNAP–Fdx clamp (yellow) (Protein Data Bank (PDB) ID: 6BZO). The actinobacterial-specific insert in the clamp is partially cropped. The clamp residues, β′ K314 and β′ M319, which interact with Fdx (shown in green spheres) in *Cdiff* but not in *Mtb* RNAP, are shown as red spheres. The zinc in the ZBD is shown as a blue sphere. **b**, Interactions between Fdx and *Cdiff* RNAP. Hydrogen-bonding interactions are shown as black dashed lines. The cation–π interaction of β′ R89 is shown with a red dashed line. Arches represent hydrophobic interactions. RNAP residues are coloured corresponding to subunits: cyan (β) and pink (β′). The Fdx-contacting residues that are not present in the *Mtb* $E\sigma^{A}$–Fdx structure (PDB ID: 6BZO) are marked with red circles. **c**, The sequence of the native *Cdiff* ribosomal RNAP *rrnC* promoter used in the in vitro transcription assay in **d**. The −10 and −35 promoter elements are shaded in purple and green, respectively. The abortive transcription reaction used to test Fdx effects is indicated below the sequence. *[α-^{32}P]GTP was used to label the abortive product GpUpG. **d**, Fdx inhibits *Cdiff* $E\sigma^{A}$ and *Mtb* RbpA-$E\sigma^{A}$ similarly and about 100 times more effectively than *E. coli* $E\sigma^{70}$. The transcription assays for *Cdiff* and *Mtb* were each repeated three times independently with similar results (n = 3). Data are mean ± s.d. of three replicates from one representative experiment (for some points, s.d. was smaller than the data symbols).

whereas S85 Cβ forms a nonpolar interaction with the Fdx C32 methyl group (Figs. 1b, 3, Extended Data Fig. 6a, Supplementary Table 3). We focused on β′ K84 because all species contain a Cβ at position 85, whereas position 84 displays a divergent pattern among gut commensal bacteria (Extended Data Fig. 8). For Gram-positive bacteria, which are hypersensitive to Fdx (MIC < 0.125 μg ml^{-1}), the β′ K84 position is always positively charged (K or R). However, for Gram-negative bacteria, which are resistant to Fdx (MIC > 32 μg ml^{-1}), β′ K84 is replaced by a neutral residue (Q in *E. coli* or L in *Pseudomonas aeruginosa* and *Neisseria meningitidis*; Extended Data Fig. 8). Notably, in Bacteroidetes (for example, *Bacteroides uniformis*, *Bacteroides ovatus* and *Bacteroides distasonis*), which are highly resistant to Fdx (MIC > 32 μg ml^{-1}), β′ K84 is replaced by negatively charged glutamic acid (E). In an analysis of common species present in the human gut microbiota[28,29] (Supplementary Table 4), β′ K84 is replaced by E in Bacteroidetes (the most abundant bacteria[30,31]) and by neutral residues (Q, T or S) in Proteobacteria (Fig. 4a, Extended Data Fig. 9). We thus refer to β′ K84 as the Fdx sensitizer and propose that it is crucial for tight Fdx binding in two ways: first, by forming a salt bridge (a proton-mediated ionic interaction) between the positively charged ε-amino group of β′ K84 and a negatively charged phenolic oxygen of Fdx; and second, by rigidifying the α-helix of the ZBD and thus facilitating backbone hydrophobic and hydrogen-bonding interactions with downstream residues S85 (A85 in *Mtb*) and K86 (Fig. 3, Extended Data Fig. 6).

We hypothesized that variation in the Fdx sensitizer has a key role in determining the potency of Fdx activity on RNAP from different clades. To test this hypothesis, we substituted β′ K84E, β′ K84Q and β′ K84R in *Cdiff* RNAP and β′ Q94K in *E. coli* RNAP and compared their inhibition by Fdx using the *Cdiff rrnC* abortive initiation assay (Fig. 4b, c, Extended Data Fig. 10a, b). Fdx inhibits *Cdiff* wild-type (WT), β′ K84Q and β′ K84R RNAPs at similar sub-micromolar concentrations. However, inhibition of *Cdiff* β′ K84E RNAP requires a tenfold higher concentration of Fdx than the WT, indicating greater resistance to Fdx (Fig. 4b, Extended Data Fig. 10a). This result is consistent with our hypothesis that the negatively charged carboxyl group on the side chain of β′ K84E repels the negative oxygen of Fdx and disrupts the polar interaction, whereas the β′ K84Q must be less disruptive to the *Cdiff* RNAP–Fdx interaction, possibly because the glutamine is capable of forming a hydrogen bond with Fdx.

To test the effect of positive versus neutral charge at the Fdx sensitizer in the context of an RNAP that is relatively Fdx-resistant, we compared WT and β′ Q94K *E. coli* RNAPs. The *E. coli* β′ Q94K substitution creates a positive charge at this position and markedly increases sensitivity to Fdx (the IC50 decreased by a factor of 20; Fig. 4c, Extended Data Fig. 10b). This result indicates that the lack of positive charge at the sensitizer position is indeed a crucial contributor to resistance to Fdx in Proteobacteria and posed a notable discrepancy with the lack of effect of the *Cdiff* β′ K84Q substitution. We hypothesize that other differences between *Cdiff* and *E. coli* RNAP, such as the relative flexibilities of the ZBD and clamp, enable *Cdiff* RNAP, but not *E. coli* RNAP, to sustain stronger interactions when the key position is neutral (Q). However, when a negative charge (E) is present at the sensitizer position, the repulsion between the carboxylic side chain (present in Bacteroidetes) and the Fdx phenolic oxygen leads to Fdx resistance.

To test whether the Fdx sensitizer is crucial for Fdx susceptibility in vivo, we introduced a point mutation (R84E) within the native *rpoC* gene of *B. subtilis*. *B. subtilis* belongs to the same phylum (Firmicutes) as *Cdiff*. Similar to *Cdiff* and *Mtb*, it has a positively charged residue (R) at the sensitizer position but is a genetically tractable model. The *B. subtilis* WT strain was readily inhibited by 10 μM Fdx whereas the *rpoC*-R84E mutant required higher concentrations (100 μM and above) for similar inhibition (Fig. 4d). Notably, at 500 μM Fdx, the inhibition zone for the *rpoC*-R84E mutant remained significantly smaller than that for WT *B. subtilis*, whereas a control (spectinomycin) that does not target RNAP gave equivalent-sized inhibition zones. We conclude that the Fdx-sensitizing residue in RNAP, K84 in *Cdiff* and R84 in *B. subtilis*, is a key determinant of Fdx susceptibility in Firmicutes.

Similarly, to interrogate Gram-negative bacteria lacking positive charge at the sensitizer position, we tested whether a β′ Q94K

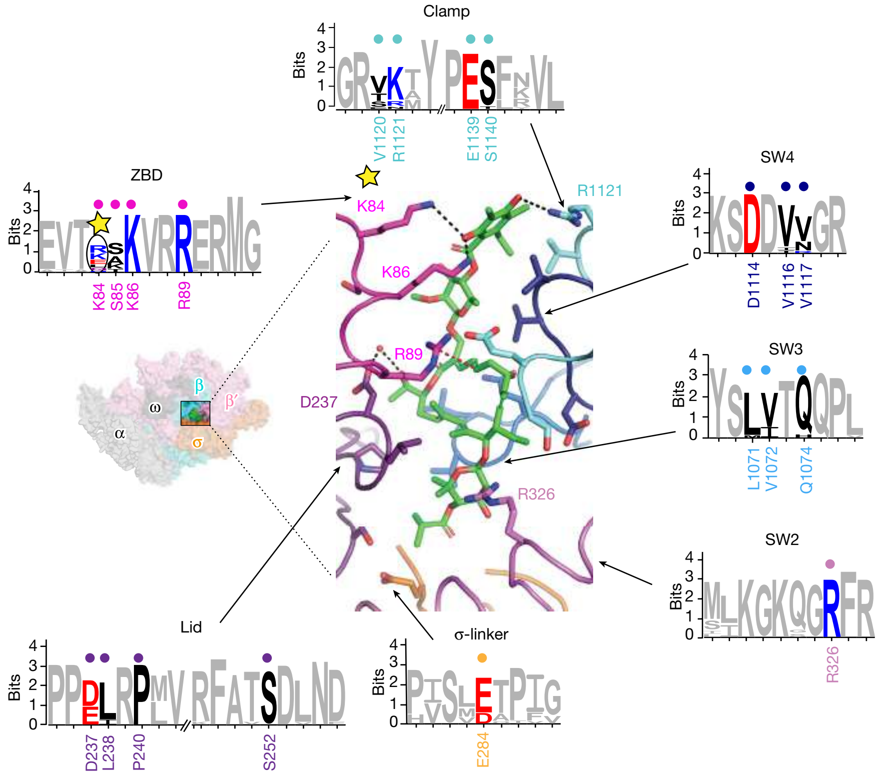

Fig. 3 | Analysis of Fdx-interacting residues across bacterial lineages. *Cdiff* RNAP Eσ^A–Fdx is shown as a molecular surface for orientation (left inset). The boxed region is magnified on the right with RNAP subunits shown as α-carbon backbone worms, Fdx-interacting residues conserved between *Mtb* and *Cdiff* shown as side-chain sticks, and Fdx (green) is shown as sticks. Non-carbon atoms are red (oxygen) and blue (nitrogen). The Fdx-interacting residues that are conserved between *Mtb* and *Cdiff* shown in the cartoon structure are labelled under the sequence logos. Amino acids that make hydrophilic interactions with Fdx are labelled on the structure. Representative bacterial species with published Fdx MICs were used to make the logos[25]. See Extended Data Fig. 8 for detailed sequence alignments. Most Fdx-interacting residues are conserved, except for residues corresponding to *Cdiff* β′ S85 and the sensitizer (indicated by the yellow star, corresponding to *Cdiff* RNAP β′ K84).

substitution could endow Fdx sensitivity to *E. coli* in vivo (Extended Data Fig. 10c, Methods). Given that the Gram-negative outer membrane is a known barrier to Fdx, we sought to test whether Fdx resistance depends on the outer-membrane barrier alone, the non-positively charged sensitizer residue on RNAP, or both using a well-characterized outer-membrane weakener, SPR741 (related to the natural antibiotic colistin produced by a Firmicute)[32,33]. Neither SPR741 nor Fdx alone had large effects on *E. coli* (Extended Data Fig. 10d). However, clear zones of inhibition were observed for the *rpoC*-Q94K mutant only at Fdx concentrations from 0.25 mM to 3 mM in the presence of SPR741 but not for the WT *E. coli* strain, even at the highest Fdx concentration (Fig. 4e). Although the extent to which outer-membrane weakeners may be present in the gut microbiome is unknown, we note that colistin is just one of many natural antibiotics produced by competing microbes and that medicinal antibiotics are often administered in combination. We conclude that both the outer membrane and the lack of positive charge at the sensitizer position of RNAP contribute to Fdx resistance in a Gram-negative bacterium under conditions that are likely to be relevant to the gut microbiome. Conversely, a positively charged sensitizer (as found in *Cdiff* and *Mtb*) is crucial for conferring Fdx sensitivity. Thus our studies enable the rational optimization of Fdx, depending on the target pathogen. For example, one might be able to substitute the phenolic oxygen with a stronger acid to treat Gram-positive pathogens or with a basic group to treat Gram-negative pathogens.

In summary, our high-resolution structure of *Cdiff* RNAP Eσ^A reveals features that are likely to be specific to Clostridia and, to some extent Firmicutes and Gram-positive bacteria. Analysis of this structure, in combination with bioinformatics and structure-guided functional assays, revealed a 'sensitizing' determinant for Fdx, a single amino-acid residue in the ZBD of the RNAP β′ subunit. This work shows how Fdx selectively targets *Cdiff* versus beneficial gut commensals such as Bacteroidetes. Although wide-spectrum antibiotics are broadly effective therapies, our results highlight the advantages of narrow-spectrum antibiotics to treat intestinal infections and probably other bacterial infections. Treatment by narrow-spectrum antibiotics would reduce widespread antibiotic resistance and reduce the side effects caused by the collateral eradication of the beneficial bacteria in the gut microbiome. Using a similar approach to the one applied here, further elucidation of diverse bacterial RNAP structures and mechanisms can provide a blueprint for designer antibiotics that leverage natural microbial competition to combat pathogens more effectively.

Online content

Any methods, additional references, Nature Research reporting summaries, source data, extended data, supplementary information, acknowledgements, peer review information; details of author contributions and competing interests; and statements of data and code availability are available at https://doi.org/10.1038/s41586-022-04545-z.

1. CDC. *Antibiotic Resistance Threats in the United States, 2019* (U.S. Department of Health and Human Services, CDC 2019); https://www.cdc.gov/drugresistance/pdf/threats-report/2019-ar-threats-report-508.pdf
2. Louie, T. J. et al. Fidaxomicin versus vancomycin for *Clostridium difficile* infection. *N. Engl. J. Med.* **364**, 422–431 (2011).
3. Crawford, T., Huesgen, E. & Danziger, L. Fidaxomicin: a novel macrocyclic antibiotic for the treatment of *Clostridium difficile* infection. *Am. J. Health Syst. Pharm.* **69**, 933–943 (2012).

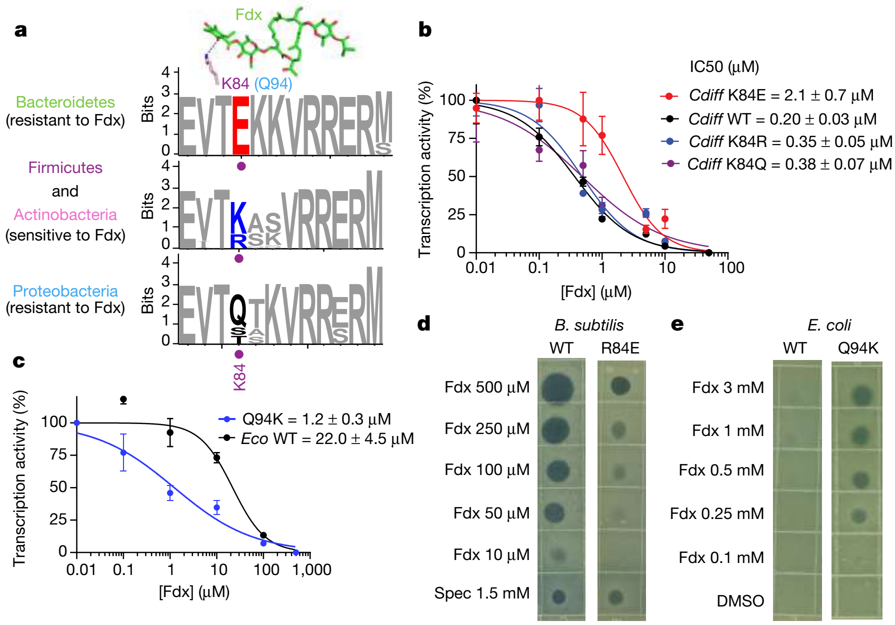

Fig. 4 | The sensitizer position (*Cdiff* RNAP β′ K84) explains Fdx narrow-spectrum activity in the gut microbiota. a, Sequence logos for the Fdx-interaction region of the β′ ZBD is highly conserved among the four most common bacterial phyla in the human microbiota: Bacteroidetes, Firmicutes, Actinobacteria and Proteobacteria, except for the sensitizer position and the C-adjacent residue (β′ K84 and S85 in *Cdiff* RNAP). The logos were derived using 66 representative species in the human microbiota[28,29] (Extended Data Fig. 9, Supplementary Table 4). **b**, Fdx effects on abortive transcription reveal that the β′ K84E substitution increases resistance tenfold, whereas β′ K84Q and β′ K84R have much smaller effects. **c**, Transcription assays with *E. coli* Eσ^{70} show the β′ Q94K substitution in *E. coli* RNAP reduces the IC50 for Fdx by a factor of approximately 20 relative to the WT enzyme. In **b**, **c**, transcription assays for each protein were repeated three times independently with similar results ($n = 3$). Data are mean ± s.d. of three replicates from one representative experiment (for some points, s.d. was smaller than the data symbols). **d**, Zone-of-inhibition assays with WT and β′ R84E *B. subtilis* demonstrate that the R84E mutation increases Fdx resistance and establishes this residue as a sensitizing determinant in vivo. The mutant (right) displayed reduced zones of inhibition relative to the WT (left) bacteria for Fdx but not for a control (spec, spectinomycin). **e**, Zone-of-inhibition assays show that the β′ Q94K substitution sensitizes *E. coli* to Fdx in the presence of the outer-membrane-weakening compound SPR741 (45 µM). WT *E. coli* (left) was not inhibited by high concentrations of Fdx (3 mM), whereas the β′ Q94K cells (right) produced zones of inhibition at 250 µM Fdx.

4. Louie, T. J., Emery, J., Krulicki, W., Byrne, B. & Mah, M. OPT-80 eliminates *Clostridium difficile* and is sparing of bacteroides species during treatment of *C. difficile* infection. *Antimicrob. Agents Chemother.* **53**, 261–263 (2009).
5. Lee, Y. J. et al. Protective factors in the intestinal microbiome against *Clostridium difficile* infection in recipients of allogeneic hematopoietic stem cell transplantation. *J. Infect. Dis.* **215**, 1117–1123 (2017).
6. Vincent, C. & Manges, A. R. Antimicrobial use, human gut microbiota and *Clostridium difficile* colonization and infection. *Antibiotics* **4**, 230–253 (2015).
7. Boyaci, H. et al. Fidaxomicin jams *Mycobacterium tuberculosis* RNA polymerase motions needed for initiation via RbpA contacts. *eLife* **7**, e34823 (2018).
8. Lin, W. et al. Structural basis of transcription inhibition by fidaxomicin (lipiarmycin A3). *Mol. Cell* **70**, 60–71.e15 (2018).
9. Morichaud, Z., Chaloin, L. & Brodolin, K. Regions 1.2 and 3.2 of the RNA polymerase σ subunit promote DNA melting and attenuate action of the antibiotic lipiarmycin. *J. Mol. Biol.* **428**, 463–476 (2016).
10. Tupin, A., Gualtieri, M., Leonetti, J. P. & Brodolin, K. The transcription inhibitor lipiarmycin blocks DNA fitting into the RNA polymerase catalytic site. *EMBO J.* **29**, 2527–2537 (2010).
11. Boyaci, H., Chen, J., Jansen, R., Darst, S. A. & Campbell, E. A. Structures of an RNA polymerase promoter melting intermediate elucidate DNA unwinding. *Nature* **565**, 382–385 (2019).
12. Chen, J., Boyaci, H. & Campbell, E. A. Diverse and unified mechanisms of transcription initiation in bacteria. *Nat. Rev. Microbiol.* **19**, 95–109 (2021).
13. Lane, W. J. & Darst, S. A. Molecular evolution of multisubunit RNA polymerases: sequence analysis. *J. Mol. Biol.* **395**, 671–685 (2010).
14. Mani, N., Dupuy, B. & Sonenshein, A. L. Isolation of RNA polymerase from *Clostridium difficile* and characterization of glutamate dehydrogenase and rRNA gene promoters in vitro and in vivo. *J. Bacteriol.* **188**, 96–102 (2006).
15. Cardone, G., Heymann, J. B. & Steven, A. C. One number does not fit all: mapping local variations in resolution in cryo-EM reconstructions. *J. Struct. Biol.* **184**, 226–236 (2013).
16. Bae, B. et al. Phage T7 Gp2 inhibition of *Escherichia coli* RNA polymerase involves misappropriation of σ^{70} domain 1.1. *Proc. Natl Acad. Sci. USA* **110**, 19772–19777 (2013).
17. Pei, H. H. et al. The δ subunit and NTPase HelD institute a two-pronged mechanism for RNA polymerase recycling. *Nat. Commun.* **11**, 6418 (2020).
18. Fang, C. et al. The bacterial multidrug resistance regulator BmrR distorts promoter DNA to activate transcription. *Nat. Commun.* **11**, 6284 (2020).
19. Campbell, E. A. et al. Structure of the bacterial RNA polymerase promoter specificity σ subunit. *Mol. Cell* **9**, 527–539 (2002).
20. Hubin, E. A. et al. Structure and function of the mycobacterial transcription initiation complex with the essential regulator RbpA. *eLife* **6**, e22520 (2017).
21. Chen, J. et al. 6S RNA mimics B-form DNA to regulate *Escherichia coli* RNA polymerase. *Mol. Cell* **68**, 388–397.e386 (2017).
22. Feklistov, A. et al. RNA polymerase motions during promoter melting. *Science* **356**, 863–866 (2017).
23. Babakhani, F., Seddon, J. & Sears, P. Comparative microbiological studies of transcription inhibitors fidaxomicin and the rifamycins in *Clostridium difficile*. *Antimicrob. Agents Chemother.* **58**, 2934–2937 (2014).
24. Kuehne, S. A. et al. Characterization of the impact of rpoB mutations on the in vitro and in vivo competitive fitness of *Clostridium difficile* and susceptibility to fidaxomicin. *J. Antimicrob. Chemother.* **73**, 973–980 (2018).
25. Goldstein, E. J., Babakhani, F. & Citron, D. M. Antimicrobial activities of fidaxomicin. *Clin. Infect. Dis.* **55**, S143–S148 (2012).
26. Kurabachew, M. et al. Lipiarmycin targets RNA polymerase and has good activity against multidrug-resistant strains of *Mycobacterium tuberculosis*. *J. Antimicrob. Chemother.* **62**, 713–719 (2008).
27. Srivastava, A. et al. New target for inhibition of bacterial RNA polymerase: 'switch region'. *Curr. Opin. Microbiol.* **14**, 532–543 (2011).
28. Forster, S. C. et al. A human gut bacterial genome and culture collection for improved metagenomic analyses. *Nat. Biotechnol.* **37**, 186–192 (2019).
29. Qin, J. et al. A human gut microbial gene catalogue established by metagenomic sequencing. *Nature* **464**, 59–65 (2010).
30. Wexler, A. G. & Goodman, A. L. An insider's perspective: Bacteroides as a window into the microbiome. *Nat. Microbiol* **2**, 17026 (2017).
31. King, C. H. et al. Baseline human gut microbiota profile in healthy people and standard reporting template. *PLoS ONE* **14**, e0206484 (2019).
32. Corbett, D. et al. Potentiation of antibiotic activity by a novel cationic peptide: potency and spectrum of activity of SPR741. *Antimicrob. Agents Chemother.* **61**, e00200–17 (2017).
33. Vaara, M. et al. A novel polymyxin derivative that lacks the fatty acid tail and carries only three positive charges has strong synergism with agents excluded by the intact outer membrane. *Antimicrob. Agents Chemother.* **54**, 3341–3346 (2010).

Publisher's note Springer Nature remains neutral with regard to jurisdictional claims in published maps and institutional affiliations.

Methods

Reagents

Antibiotics and chemicals used in this study were purchased from Sigma-Aldrich or Thermo-Fisher unless noted otherwise. SPR741 was purchased from Med Chem Express (Monmouth Junction, NJ, USA). [α-^{32}P]GTP was obtained from PerkinElmer Life Sciences. GpU was from TriLink Biotechnologies. Oligonucleotides were obtained from Integrated DNA Technologies. PCR amplification was performed using Q5 or OneTaq DNA polymerases (New England Biolabs). Restriction enzymes and T4 DNA ligase were supplied by New England Biolabs. DNA sequencing was performed by Functional Biosciences.

Protein expression and purification

***Cdiff* σ^A^.** The *Cdiff* σ^A gene (Kyoto Encyclopedia of Genes and Genomes (KEGG) entry: CD630_14550) was amplified from *Cdiff* 630 chromosomal DNA and cloned between NcoI and NheI sites of pET28a plasmid. A His10 tag with a Rhinovirus 3C protease recognition site was added to the N-terminus end of the σ^A gene to facilitate purification. *E. coli* BL21(λDE3) cells were transformed with this plasmid and were induced with 0.5 mM isopropyl-beta-D-thiogalactopyranoside (IPTG) overnight at 16 °C. The protein was affinity purified on a Ni^{2+}-column (HiTrap IMAC HP, GE Healthcare Life Sciences). The column was washed with 20 column volumes of wash buffer (20 mM Tris-HCl, pH 8, 0.5 M NaCl, 5% (v/v) glycerol, 50 mM imidazole, and 1 mM dithiothreitol) to remove contaminating proteins, and the His-tagged protein was eluted with wash buffer containing 250 mM imidazole. The eluted protein was cleaved with Rhinovirus 3C protease overnight, the cleaved complex was loaded onto a second Ni^{2+} column, and the flow-through was collected and further purified by size-exclusion chromatography (Superdex 200, GE Healthcare) in 20 mM Tris-HCl, pH 8, 5% (v/v) glycerol, 1 mM EDTA, 0.5 M NaCl, and 5 mM DTT. The eluted *Cdiff* σ^A were subsequently concentrated and stored in 20 mM Tris-HCl, pH 8, 10% (v/v) glycerol, 0.3 M NaCl, and 5 mM DTT at −80 °C.

***Cdiff* RNAP.** The *Cdiff* RNAP overexpression plasmid was constructed in multiple steps. First, the *Cdiff 630 rpoA* (KEGG: CD630_00980), *rpoZ* (KEGG: CD630_25871), *rpoB* (KEGG: CD630_00660), and *rpoC* (KEGG: CD630_00670) genes were codon-optimized for *E. coli* using Gene Designer (ATUM) and codon frequencies reported by Welch et al.[34]. A strong ribosome-binding site (RBS) was designed for each gene using the Salis RBS design tools[35]. DNA fragments containing the *rpoA, rpoZ, rpoB* and *rpoC* genes and the RBSs were purchased from Integrated DNA Technologies and assembled into pET21 (Novagen) by Gibson assembly (NEB HiFi). To ensure 1:1 stoichiometry and inhibit assembly with the host *E. coli* subunits, β and β′ were fused using a polypeptide linker (LARHGGSGA), a method previously used for overexpression of *Mtb* RNAP[36]. A His_{10} tag preceded by a Rhinovirus 3C protease cleavable site was added to the C-terminus of *rpoC* to facilitate purification, resulting in plasmid pXC026. The plasmids encoding *Cdiff* RNAP mutants (*rpoC*-K84E, K84R and K84Q) were constructed by Q5 site-directed mutagenesis (NEB Q5 Site-Directed Mutagenesis Kit Quick Protocol using pXC026 as the template). Overexpression of *Cdiff* RNAP yielded high levels of proteolysis and inclusion bodies in the conventional BL21 λDE3 strain. Yields of soluble, intact *Cdiff* RNAP were increased in *E. coli* B834(λDE3), a strain reported to overproduce intact *B. subtilis* RNAP[37]. *Cdiff* core RNAP was co-overexpressed in *E. coli* B834(λDE3) (Novagen) overnight at 16 °C for approximately 16 h after induction with 0.3 mM IPTG in LB medium with 50 μg ml^{-1} kanamycin. The cell pellet was resuspended in the lysis buffer (50 mM Tris-HCl pH 8.0, 1 mM EDTA, 5% (v/v) glycerol, 5 mM 1,4-dithiothreitol (DTT), 1× protease inhibitor cocktail (Halt Protease Inhibitor Cocktail (100×), Thermo Fisher), and 1 mM phenylmethylsulfonyl fluoride (PMSF). Cells were lysed by continuous flow through a French press (Avestin) and spun twice at 11,000*g*, 20 min, 4 °C. DNA and RNAP were precipitated from the supernatant by gradual addition with mixing of polyethyleneimine (PEI) to 0.6% w/v final concentration. After centrifugation at 11,000*g*, 20 min, 4 °C, the PEI pellets were washed three times with 10 mM Tris-HCl, pH 8, 0.25 M NaCl, 0.1 mM EDTA, 5 mM DTT, and 5% (v/v) glycerol, and the RNAP was then eluted three times with a solution of the same composition but with 1 M NaCl. The RNAP was precipitated overnight with gentle stirring at 4 °C after gradual addition of ammonium sulfate to 35% (w/v) final concentration. After centrifugation at 11,000*g*, 25 min, 4 °C, the RNAP was resuspended in 20 mM Tris-HCl, pH 8, 5% (v/v) glycerol, 0.5 M NaCl, and 5 mM β-mercaptoethanol and subjected to Ni^{2+}-affinity chromatography purification. The column was washed with 20 column volumes of wash buffer (20 mM Tris-HCl, pH 8, 0.5 M NaCl, 5% (v/v) glycerol, 50 mM imidazole, and 5 mM β-mercaptoethanol) to remove contaminating proteins, and eluted with wash buffer containing 250 mM imidazole. The eluted protein was cleaved with Rhinovirus 3C protease overnight. The cleaved protein was loaded onto a second Ni^{2+} column, and the flow-through was collected, concentrated, dialysed overnight in 20 mM Tris-HCl pH 8.0, 20% (v/v) glycerol, 0.1 mM EDTA, 0.5 M NaCl and 1 mM DTT, and then stored at −80 °C.

In vitro transcription assays

The *Cdiff rrnC* promoter DNA template (see below for sequences) was PCR amplified from genomic DNA of *Cdiff 630*, phenol extracted, diluted to 200 nM in 10 mM Tris-HCl (pH 7.9), and stored at −20 °C. Transcription assays were performed in 20 μL reactions as described previously[38]. In brief, 50 nM of *Cdiff* or *E. coli* WT or mutant RNAP Eσ^A was combined in transcription buffer (10 mM Tris HCl, pH 7.9, 50 mM KCl, 10 mM $MgCl_2$, 0.1 mM DTT, 5 μg ml^{-1} bovine serum albumin and 0.1 mM EDTA) with different concentrations of Fdx (0.01–500 μM; final reaction volumes after addition of DNA and NTPs were 20 μl). The mixtures were incubated at 37 °C for 5 min to allow for the antibiotic to bind. The dsDNA fragment containing the *Cdiff rrnC* promoter (GenBank: CP010905.2) was added (10 nM final) to each tube and the samples were incubated for an additional 15 min at 37 °C to allow the formation of the RNAP open complex. Dinucleotide (GpU, 20 μM) was added and incubation was continued for 10 min. Transcription was initiated by addition of [α-^{32}P]GTP to a final concentration of 10 μM (4.2 Ci mmol^{-1}), allowed to proceed for 10 min at 37 °C, and stopped by the addition of 20 μl of 2× stop buffer (90 mM Tris-borate buffer pH 8.3, 8 M urea, 30 mM EDTA, 0.05% bromophenol blue, and 0.05% xylene cyanol). The samples were heated at 95 °C for 1 min and then loaded onto a polyacrylamide gel (20% Acrylamide/Bis acrylamide (19:1), 6 M urea, and 45 mM Tris-borate, pH 8.3, 1.25 mM Na_2EDTA). Transcription products were visualized by phosphorimaging using a Typhoon FLA 9000 (GE Healthcare) and quantified using ImageQuant software (GE Healthcare). Quantified values were plotted in PRISM and the IC50 was calculated from three independent data sets. The full sequences of the fragments (initiation sites in lowercase, −35 and −10 elements in bold) used for transcription are as follows. *rrnC* promoter (sequences used as PCR primers are underlined): <u>AATAGCTTGTATTAAAGCAGTTA</u>AAATGCATTAATATAGG CTATTTTTATTTTGACAAAAAAATATTTAAAATAAAAGTTAAAAAGTTG **TTGACT**TAGAATAATATAGATGA**TATTAT**ATATGA**gtg**CCCAAAAGGAG CACCAAAATAAGACAAAA<u>GAACTTTGAAAATTAAACAGTA</u>.

Preparation of WT *Cdiff* Eσ^A for cryo-EM

The RNAP core was incubated with 15 molar excess of σ^A for 15 min at 37 °C and 45 min at 4 °C. The complex was then purified over a Superose 6 Increase 10/300 GL column (GE Healthcare) in gel filtration buffer (20 mM Tris-HCl pH 8.0, 150 mM potassium glutamate, 5 mM $MgCl_2$, 2.5 mM DTT). The eluted RNAP Eσ^A was concentrated to 6 mg ml^{-1} (14 μM) by centrifugal filtration (Amicon Ultra). Eσ^A was mixed with 100 μM final concentration of Fdx (10 mM stock solution in DMSO) and incubated for 15 min at 4 °C.

Cryo-EM grid preparation

Before freezing cryo-EM grids, octyl β-D-glucopyranoside was added to the samples to a final concentration of 0.1% (ref. [8]). C-flat holey carbon grids (CF-1.2/1.3-4Au, Protochips) were glow-discharged for 20 s before the application of 3.5 µl of the samples. Using a Vitrobot Mark IV (Thermo Fisher Scientific Electron Microscopy), grids were blotted and plunge-frozen in liquid ethane with 100% chamber humidity at 22 °C.

Cryo-EM data acquisition and processing

Structural biology software was accessed through the SBGrid consortium[39]. *Cdiff* Eσ^A with Fdx grids were imaged using a 300 keV Titan Krios (Thermo Fisher Scientific Electron Microscopy) equipped with a K3 Summit direct electron detector (Gatan). Dose-fractionated movies were recorded in counting mode using Leginon at a nominal pixel size of 1.083 Å per pixel (micrograph dimensions of 5,760 × 4,092 pixels) over a nominal defocus range of −1 µm to −2.5 µm (ref. [40]). Movies were recorded in 'counting mode' (native K3 camera binning 2) with a dose rate of 30 electrons per physical pixel over a total exposure of 2 s (50 subframes of 0.04 s) to give a total dose of about 51 e^- Å^{-2}. A total of 6,930 movies were collected. Dose-fractionated movies were gain-normalized, drift-corrected, summed, and dose-weighted using MotionCor2[41]. The contrast transfer function was estimated for each summed image using Patch contrast transfer function (CTF) module in cryoSPARC v2.15.0[42]. cryoSPARC Blob Picker was used to pick particles (no template was supplied). A total of 2,502,242 particles were picked and extracted from the dose-weighted images in cryoSPARC using a box size of 256 pixels. Particles were sorted using cryoSPARC 2D classification (number of classes, N = 50), resulting in 2,415,902 curated particles. Initial models (reference 1: RNAP, reference 2: decoy 1 and reference 3: decoy 2) were generated using cryoSPARC ab initio reconstruction[42] on a subset of 81,734 particles. Particles were further curated using references 1 to 3 as 3D templates for cryoSPARC Heterogeneous Refinement (N = 6), resulting in the following: class 1 (reference 1), 460,464 particles; class 2 (reference 1), 641,091 particles; class 3 (reference 2), 296,508 particles; class 4 (reference 2), 203,296 particles; class 5 (reference 3), 390,575 particles; class 6 (reference 3), 327,065 particles. Particles from class 1 and class 2 were combined and further curated with another round of heterogeneous refinement (N = 6), resulting in the following: class 1 (reference 1), 185,262 particles; class 2 (reference 1), 394,040 particles; class 3 (reference 2), 110,023 particles; class 4 (reference 2), 110,743 particles; class 5 (reference 3), 104,013 particles; class 6 (reference 3), 124,547 particles. Curated particles from class 2 were refined using cryoSPARC non-uniform refinement[42] and then further processed using RELION 3.1-beta Bayesian polishing[43]. Per-particle CTFs were estimated for the polished particles using cryoSPARC Homogeneous Refinement with global and local CTF refinement enable[42]. These particles were further curated using cryoSPARC heterogeneous refinement (N = 3), resulting in the following: class 1 (reference 1), 85,470 particles; class 2 (reference 1), 231,310 particles; class 3 (reference 1), 77,250 particles. Particles from class 2 were selected for a subsequent cryoSPARC heterogeneous refinement (N = 3), resulting in the following: class 1 (reference 1), 19,282 particles; class 2 (reference 1), 182,390 particles; class 3 (reference 1), 29,638 particles. Particles in class 2 were refined using cryoSPARC non-uniform refinement[44], resulting in final 3D reconstruction containing 182,390 particles with nominal resolution of 3.26 Å. Local resolution calculations were generated using blocres and blocfilt from the Bsoft package[45].

Model building and refinement

A homology model for *Cdiff* Eσ^A was derived using SWISS-MODEL[46] and PDBs: 5VI5[20] for αI and αII; 6BZO[7] for β, β', and σ^A; and 6FLQ[47] for ω. The homology model was manually fit into the cryo-EM density maps using Chimera[48] and rigid-body and real-space refined using Phenix[49]. A model of Fdx was used from the previous structure PDB ID: 6BZO to place in the cryo-EM map[7]. Rigid body refinement for rigid domains of RNAP was performed in PHENIX. The model was then manually adjusted in Coot[50] and followed by all-atom and B-factor refinement with Ramachandran and secondary structure restraints in PHENIX. The BBM2 modules were built using AlphaFold2 model[51]. The refined model was 'shaken' by introducing random shifts to the atomic coordinates with root mean squared deviation of 0.163 Å in phenix.pdbtools[49]. The shaken model was refined into half-map1 and Fourier shell correlations (FSCs) were calculated between the refined shaken model and half-map 1 (FSChalf1 or work), half-map 2 (FSChalf2 or free, not used for refinement), and combined (full) maps using phenix.mtriage[52]. Unmasked log files were plotted in PRISM and the FSC − 0.5 was calculated for the full map.

Construction of *E. coli* and *B. subtilis* mutant strain. Site-directed mutagenesis was performed on the *E. coli rpoC* IPTG-inducible expression plasmid pRL662[53] using Q5 site-directed mutagenesis (NEB Q5 Site-Directed Mutagenesis Kit Quick Protocol) to construct pRL662-Q94K. Plasmids pRL662 and pRL662-Q94K were each transformed into the temperature-sensitive strain RL602 (*rpoC*(Am) supD43,74(Ts))[54], which is unable to produce RNAP or grow at ≥39 °C.

To introduce the *rpoC*-R84E mutation into *B. subtilis*, a CRISPR–Cas9 method[55] was used to produce strain RL3914. Upstream and downstream fragments (1 kb each) flanking the point mutation site were PCR amplified and then combined with the guide RNA segment (5′-AGTTTGTGACCGCTGCGGAGTCGAAGTAACA-3′) using annealed, complementary oligonucleotides (IDT) in a plasmid backbone from pJW557 (gift J. Wang) as described[55]. The resulting plasmid, pXC052, was then transformed into RL3915 (an *E. coli recA*$^+$ strain) for multimerization. Multimerized pXC052 was obtained by conventional plasmid miniprep, and transformed into *B. subtilis* 168, and incubated at 30 °C overnight on LB plate with 100 µg ml^{-1} spectinomycin added. Single colonies were picked the next day and cured of plasmid by growth at 45 °C for 24 h on an LB plate. The genomic *rpoC*-R84E point mutation was verified by colony PCR and Sanger sequencing.

Fdx inhibition assay on agar plates. Fdx zone-of-inhibition assays for both *E. coli* and *B. subtilis* were performed on agar plates using the soft-agar overlay technique[56]. Single colonies of *E. coli* RL602/pRL662 and RL602/pRL662-Q94K strains were inoculated into LB broth (5 ml) containing 100 µg ml^{-1} ampicillin plus 0.3 mM IPTG (to induce expression of *rpoC*) and incubated at 42 °C with shaking to apparent OD_{600} of 0.4–0.6. Approximately 0.05 OD_{600} units of cells were then mixed with 4 ml soft overlay agar (0.4 %) at 55 °C, poured onto an LB 1.5% agar plate containing 100 µg ml^{-1} ampicillin and 0.5 mM IPTG (to maintain *rpoC* expression), and allowed to solidify at 25 °C. Test compounds in DMSO or H_2O (3 µl) were then spotted onto solidified overlay agar and the plates were incubated overnight at 42 °C before scoring the zones of inhibition. For the *B. subtilis* 168 (WT) and *rpoC*-R84E strains, the cell cultures and bottom agar did not contain antibiotic or IPTG and the plates were incubated overnight at 37 °C before scoring. Fdx, rifampicin (Rif), and SPR741 were prepared in 100% DMSO. Spectinomycin (Spec) and kanamycin (Kan) were prepared in H_2O.

Reporting summary

Further information on research design is available in the Nature Research Reporting Summary linked to this paper.

Data availability

Cryo-EM maps and atomic models generated in this paper have been deposited in the Electron Microscopy Data Bank (accession codes EMD-23210) and the Protein Data Bank (accession codes 7L7B). The atomic models used in this paper were obtained from the Protein Data Bank under accession codes 5VI5, 6BZO and 6FLQ. Source data are provided with this paper.

34. Welch, M. et al. Design parameters to control synthetic gene expression in *Escherichia coli*. *PLoS ONE* **4**, e7002 (2009).
35. Salis, H. M., Mirsky, E. A. & Voigt, C. A. Automated design of synthetic ribosome binding sites to control protein expression. *Nat. Biotechnol.* **27**, 946–950 (2009).

36. Czyz, A., Mooney, R. A., Iaconi, A. & Landick, R. Mycobacterial RNA polymerase requires a U-tract at intrinsic terminators and is aided by NusG at suboptimal terminators. *Mbio* **5**, e00931 (2014).
37. Yang, X. & Lewis, P. J. Overproduction and purification of recombinant *Bacillus subtilis* RNA polymerase. *Protein Expr. Purif.* **59**, 86–93 (2008).
38. Davis, E., Chen, J., Leon, K., Darst, S. A. & Campbell, E. A. Mycobacterial RNA polymerase forms unstable open promoter complexes that are stabilized by CarD. *Nucleic Acids Res.* **43**, 433–445 (2015).
39. Morin, A. et al. Collaboration gets the most out of software. *eLife* **2**, e01456 (2013).
40. Suloway, C. et al. Automated molecular microscopy: the new Leginon system. *J. Struct. Biol.* **151**, 41–60 (2005).
41. Zheng, S. Q. et al. MotionCor2: anisotropic correction of beam-induced motion for improved cryo-electron microscopy. *Nat. Methods* **14**, 331–332 (2017).
42. Punjani, A., Rubinstein, J. L., Fleet, D. J. & Brubaker, M. A. cryoSPARC: algorithms for rapid unsupervised cryo-EM structure determination. *Nat. Methods* **14**, 290–296 (2017).
43. Zivanov, J. et al. New tools for automated high-resolution cryo-EM structure determination in RELION-3. *eLife* **7**, e42166 (2018).
44. Punjani, A., Zhang, H. & Fleet, D. J. Non-uniform refinement: adaptive regularization improves single-particle cryo-EM reconstruction. *Nat. Methods* **17**, 1214–1221 (2020).
45. Heymann, J. B. & Belnap, D. M. Bsoft: image processing and molecular modeling for electron microscopy. *J. Struct. Biol.* **157**, 3–18 (2007).
46. Waterhouse, A. et al. SWISS-MODEL: homology modelling of protein structures and complexes. *Nucleic Acids Res.* **46**, W296–W303 (2018).
47. Guo, X. et al. Structural basis for NusA stabilized transcriptional pausing. *Mol. Cell* **69**, 816–827.e814 (2018).
48. Pettersen, E. F. et al. UCSF Chimera—a visualization system for exploratory research and analysis. *J. Comput. Chem.* **25**, 1605–1612 (2004).
49. Afonine, P. V. et al. Real-space refinement in PHENIX for cryo-EM and crystallography. *Acta Crystallogr. D* **74**, 531–544 (2018).
50. Emsley, P., Lohkamp, B., Scott, W. G. & Cowtan, K. Features and development of Coot. *Acta Crystallogr. D* **66**, 486–501 (2010).
51. Jumper, J. et al. Highly accurate protein structure prediction with AlphaFold. *Nature* **596**, 583–589 (2021).
52. Afonine, P. V. et al. New tools for the analysis and validation of cryo-EM maps and atomic models. *Acta Crystallogr. D* **74**, 814–840 (2018).
53. Toulokhonov, I., Zhang, J., Palangat, M. & Landick, R. A central role of the RNA polymerase trigger loop in active-site rearrangement during transcriptional pausing. *Mol. Cell* **27**, 406–419 (2007).
54. Weilbaecher, R., Hebron, C., Feng, G. & Landick, R. Termination-altering amino acid substitutions in the β′ subunit of *Escherichia coli* RNA polymerase identify regions involved in RNA chain elongation. *Genes Dev.* **8**, 2913–2927 (1994).
55. Burby, P. E. & Simmons, L. A. CRISPR/Cas9 editing of the *Bacillus subtilis* genome. *Bio. Protoc.* **7**, e2272 (2017).
56. Hockett, K. L. & Baltrus, D. A. Use of the soft-agar overlay technique to screen for bacterially produced inhibitory compounds. *J. Vis. Exp.* **119**, 55064 (2017).
57. Wallace, A. C., Laskowski, R. A. & Thornton, J. M. LIGPLOT: a program to generate schematic diagrams of protein-ligand interactions. *Protein Eng.* **8**, 127–134 (1995).
58. Stamatakis, A. RAxML-VI-HPC: maximum likelihood-based phylogenetic analyses with thousands of taxa and mixed models. *Bioinformatics* **22**, 2688–2690 (2006).
59. Letunic, I. & Bork, P. Interactive Tree Of Life (iTOL) v4: recent updates and new developments. *Nucl. Acids Res.* **47** (W1), W256–W259 (2019).

Acknowledgements We thank S. Darst for helpful discussions during this study; R. Mooney for providing σ^{70} protein for transcription assays; J. Wang for providing plasmid pJW557; M. Young and J. Yang for guidance in *B. subtilis* genetics; M. Ebrahim, J. Sotiris and Honkit Ng at The Rockefeller University Evelyn Gruss Lipper Cryo-electron Microscopy Resource Center; and E. Eng and K. Maruthi for collecting cryo-EM data. Some of this work was performed at the Simons Electron Microscopy Center and National Resource for Automated Molecular Microscopy located at the New York Structural Biology Center, supported by grants from the Simons Foundation (SF349247), NYSTAR, the Agouron Institute (F00316), and the NIH (GM103310, OD019994). This research was supported by grants from the NIH to R.L. (GM38660) and E.A.C. (GM114450) and funding from the Revson Foundation to H.B. (CEN5650030).

Author contributions E.A.C. and R.L. supervised this work. X.C. and H.B. carried out biochemical and functional assays. H.B., E.A.C. and J.C. determined the cryo-EM structures and built the structural model. X.C. performed bioinformatic analysis. Y.B. assisted with protein purifications. X.C., H.B., E.A.C. and R.L. wrote the manuscript with input from all authors.

Competing interests The authors declare no competing interests.

Additional information
Supplementary information The online version contains supplementary material available at https://doi.org/10.1038/s41586-022-04545-z.
Correspondence and requests for materials should be addressed to Robert Landick or Elizabeth A. Campbell.
Peer review information *Nature* thanks Robert Britton and the other, anonymous reviewer(s) for their contribution to the peer review of this work. Peer review reports are available.

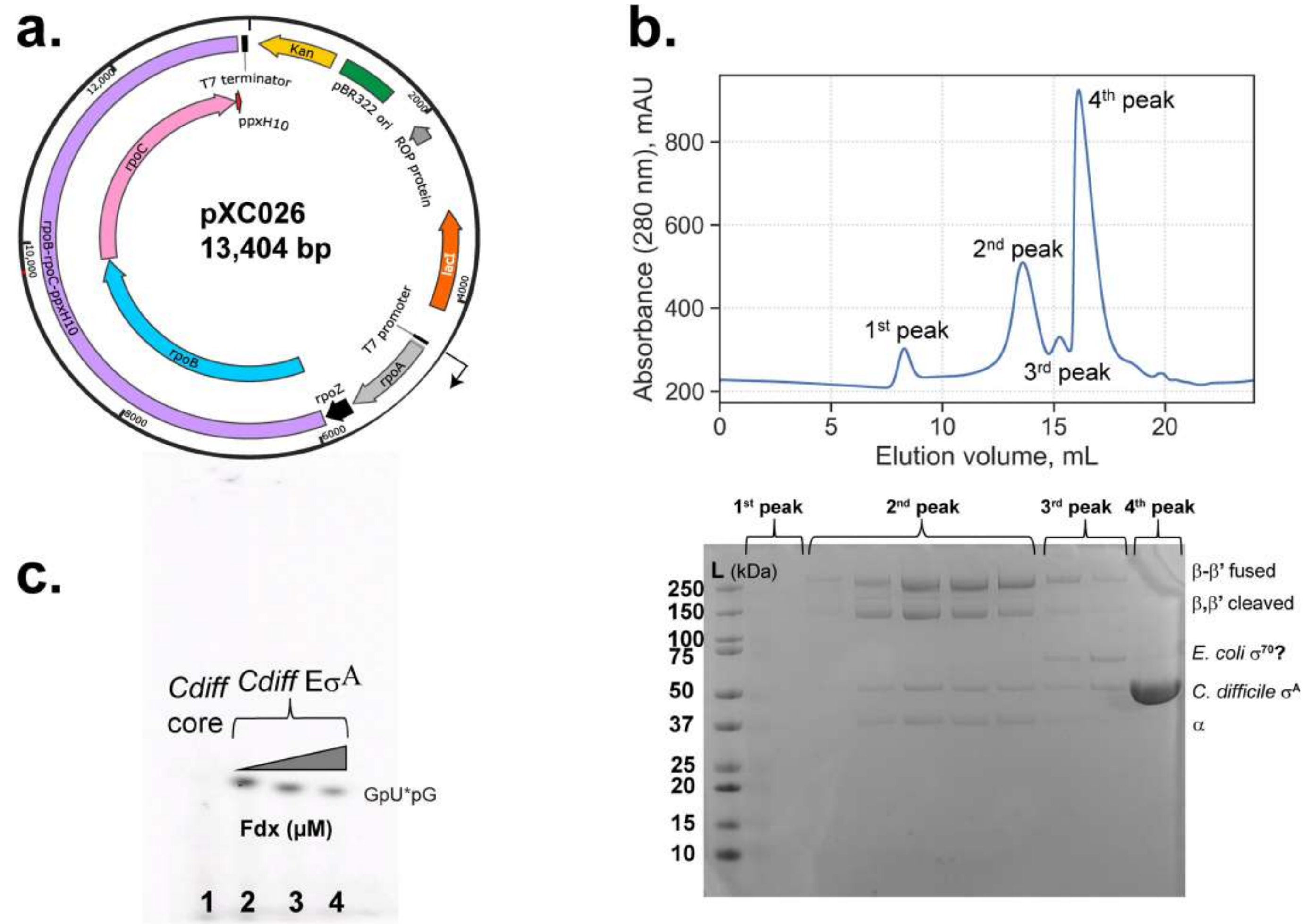

Extended Data Fig. 1 | Overexpression and purification of *Cdiff* RNAP. **a**, pXC026, overexpression plasmid for the *Cdiff* rpoA, rpoZ, rpoB, and rpoC genes (encoding the α, ω, β, and β′ subunits of *Cdiff* RNAP, respectively). The β and β′ subunits were fused with an inter-subunit 10-amino-acid (aa) linker (LARHVGGSGA) and a C-terminal Rhinovirus 3C protease-cleavable His10 tag. **b**, (Top) Size-exclusion chromatography profile for the assembled *Cdiff* RNAP $E\sigma^A$. (Bottom) Coomassie-stained SDS-PAGE of individual fractions from major peaks. RNAP subunits are labeled on the right of the gel. The yield for *Cdiff* RNAP $E\sigma^A$ from pooled fractions of the second peak was sufficient from single purification and used for biochemistry and structural biology experiments. **c**, Abortive transcription assay with *Cdiff* core and $E\sigma^A$ using the *Cdiff* rrnC promoter as DNA template. The transcriptional activity of *Cdiff* $E\sigma^A$ was inhibited with increasing concentrations of Fdx. The transcription assays were repeated three times independently with similar results (n = 3). The result is shown from one representative experiment. The result is shown from one representative experiment. Lane 1, *Cdiff* RNAP core; lane 2, *Cdiff* $E\sigma^A$; lane 3, *Cdiff* $E\sigma^A$ with 0.2 μM Fdx added; lane 4, *Cdiff* $E\sigma^A$ with 2 μM Fdx added.

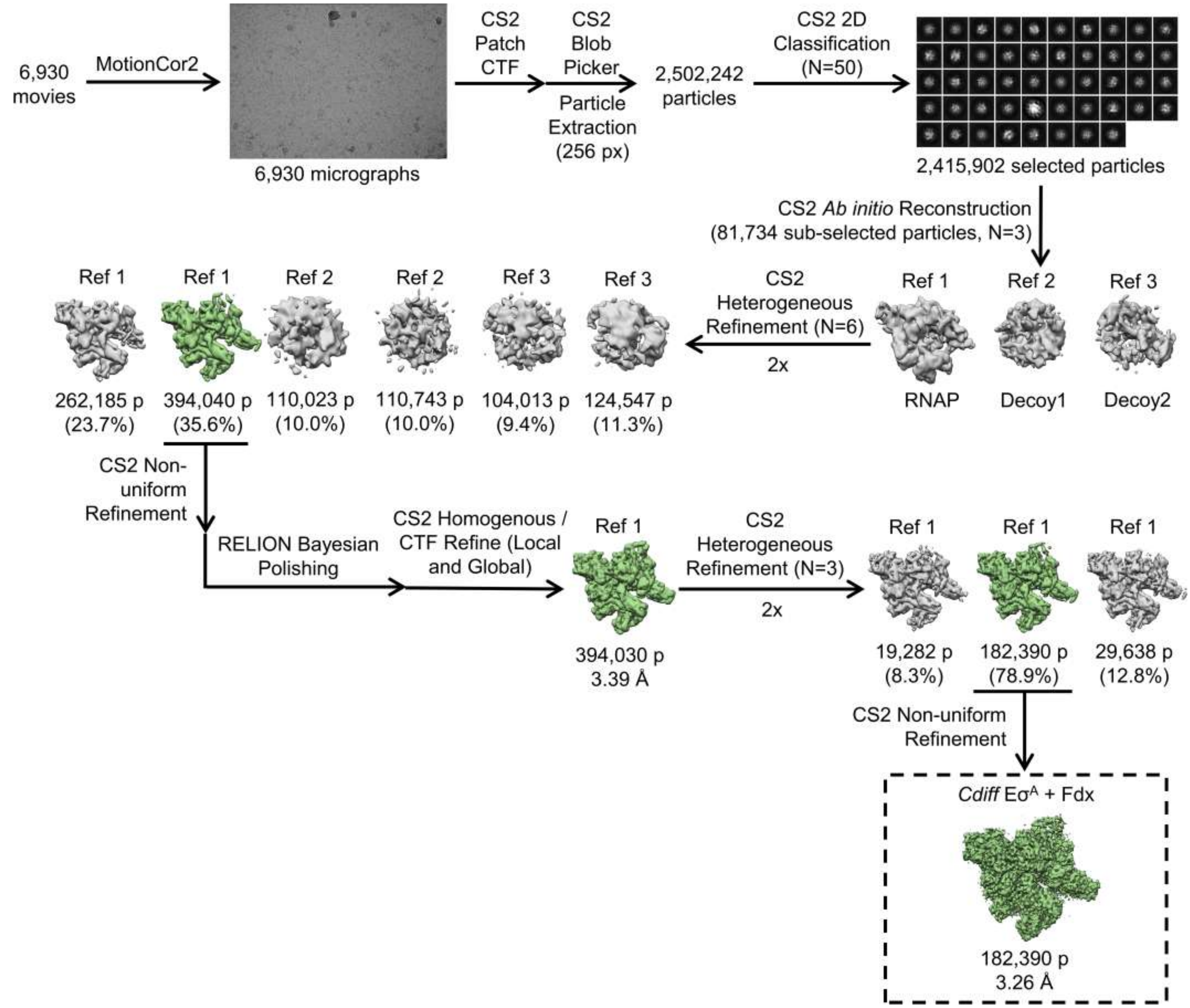

Extended Data Fig. 2 | Cryo-EM processing pipeline. Flow chart showing the image-processing pipeline for the cryo-EM data of *Cdiff* Eσ^A/Fdx complexes, starting with 6,930 dose-fractionated movies collected on a 300-keV Titan Krios (FEI) equipped with a K3 Summit direct electron detector (Gatan). Movies were frame-aligned and summed using MotionCor2[41]. CTF estimation for each micrograph was calculated with cryoSPARC2[42]. A representative micrograph is shown following processing by MotionCor2[41]. Particles were auto-picked from each micrograph with cryoSPARC2[42] Blob Picker and then sorted by 2D classification using cryoSPARC2 to assess quality. The selected classes from the 2D classification are shown. After picking and cleaning by 2D classification, the dataset contained 2,415,902 particles. A subset of particles was used to generate an *ab initio* templates in cryoSPARC2 and 3D heterogeneous refinement was performed with these templates using cryoSPARC2[42]. One major, high-resolution class emerged, which was polished using RELION[43] and further cleaned with two more 3D heterogenous refinements. The final 182,390 particles were refined using cryoSPARC Non-Uniform refinement[44].

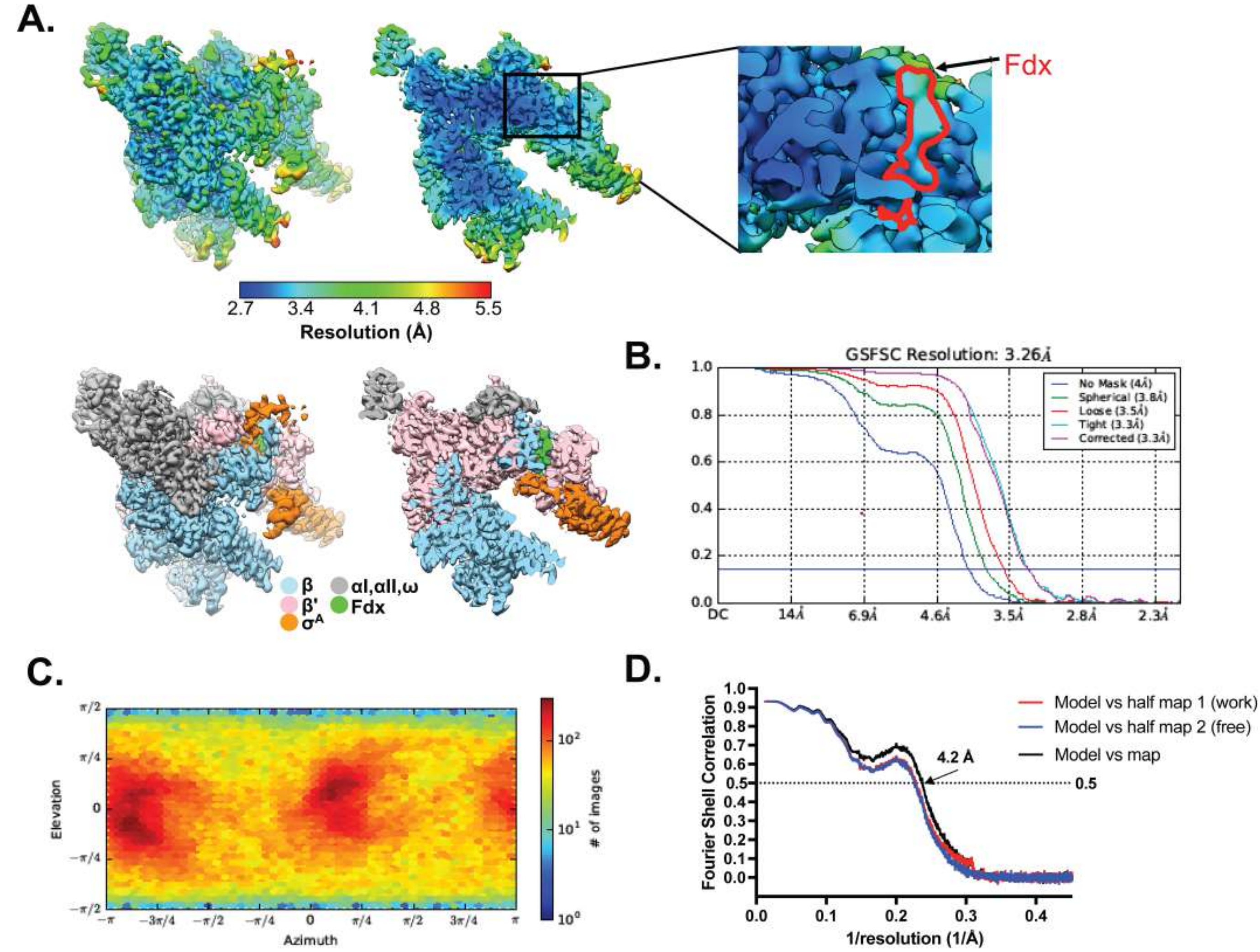

Extended Data Fig. 3 | Cryo-EM analysis. a, Top left, the 3.26 Å-resolution cryo-EM density map of *Cdiff* $E\sigma^A$/Fdx. Top right, a cross-section of the structure, showing the Fdx. Bottom, same views as above, but colored by local resolution, The boxed region is magnified and displayed as an inset. Density for Fdx is outlined in red[15]. **b**, Gold-standard FSC plots of the *Cdiff* $E\sigma^A$/Fdx complex from cryoSPARC[42]. The dotted line represents the gold-standard 0.143 FSC cutoff which indicates a nominal resolution of 3.26 Å. **c**, Angular distribution calculated in cryoSPARC for *Cdiff* $E\sigma^A$/Fdx particle projections. Heat map shows number of particles for each viewing angle (less = blue, more = red)[42]. **d**, Cross-validation FSC plots for map-to-model fitting were calculated between the refined structure of *Cdiff* $E\sigma^A$/Fdx and the half-map used for refinement (work, red), the other half-map (free, blue), and the full map (black). The dotted black line represents the 0.5 FSC cutoff determined for the full map[52].

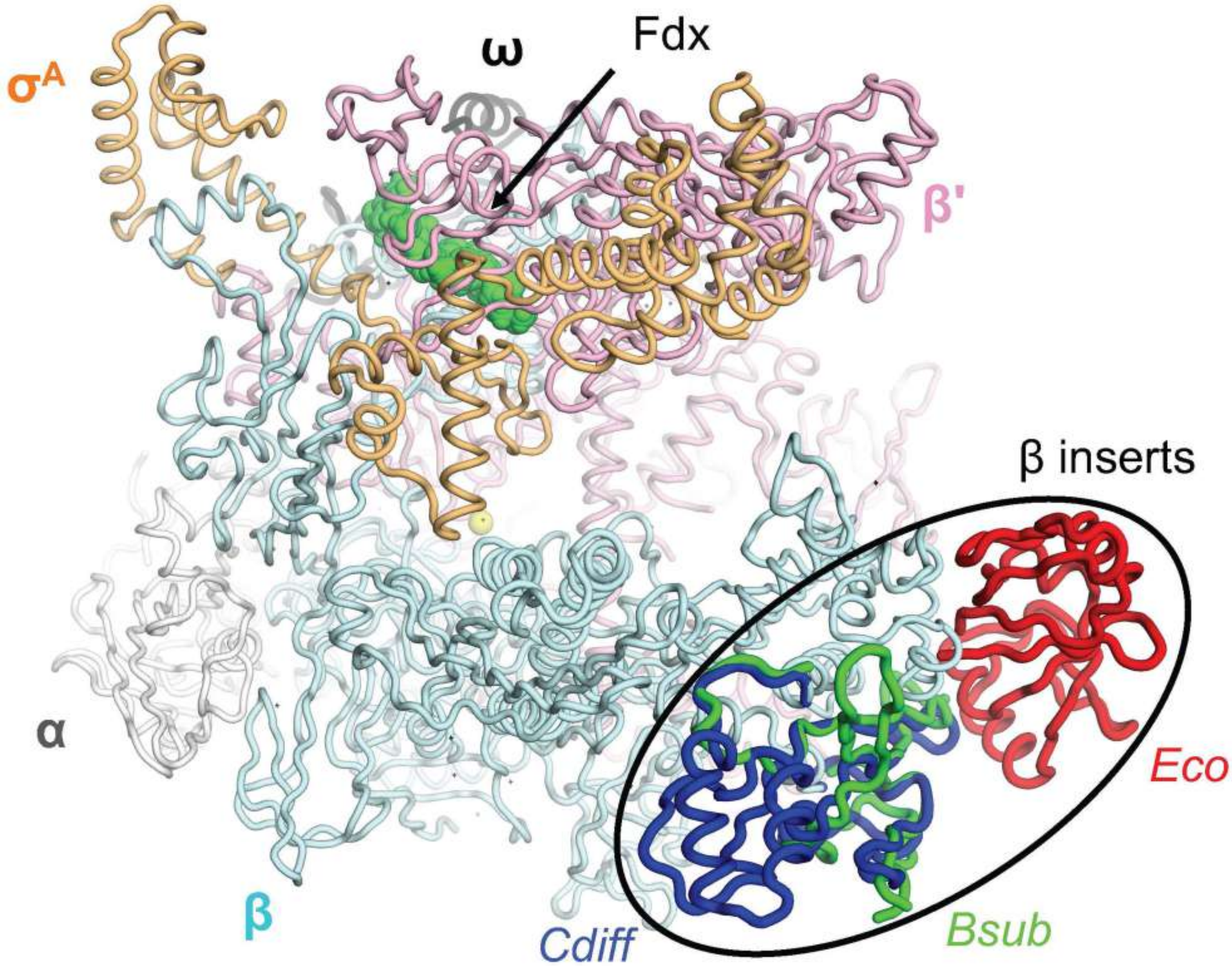

Extended Data Fig. 4 | Differences between *Cdiff* and other bacterial RNAPs. The lineage-specific β inserts are shown for *Cdiff* RNAP in dark blue, *E. coli* RNAP in red[16] (PDB ID:4LK1), *Bsub* RNAP in green[17] (PDB ID:6ZCA). The Fdx is shown in green spheres, and the active site Mg^{2+} is shown as a yellow sphere. Superimposition of the RNAPs from each organism was performed in PyMOL. Only the *Cdiff* Eσ^A is shown.

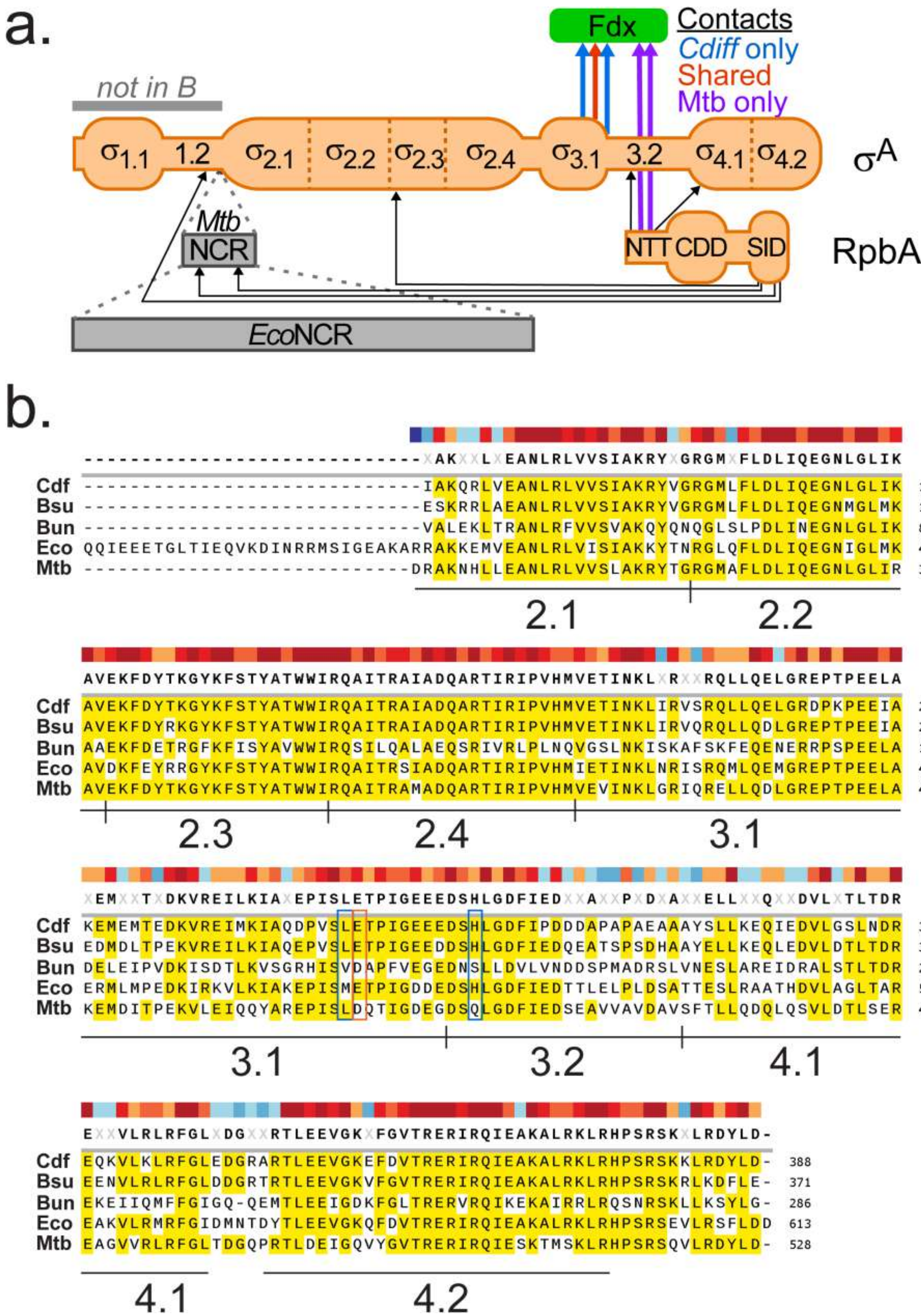

Extended Data Fig. 5 | Differences in σ^A–Fdx contacts between *Cdiff* and *Mtb* and σ^A sequence alignment. a, Conserved regions of *Cdiff* σ^A compared to *Mtb* σ^A and *E. coli* σ^{70}. *Mtb* σ^A has a much shorter σ^A NCR than *E. coli* σ^{70}, but the residues in the short *Mtb* NCR that contact RbpA are not present in either *Cdiff* or *E. coli*[20]. *Mtb* RbpA contacts Fdx whereas *Cdiff* σ^A makes more contacts to Fdx than does *Mtb* σ^A. Black arrows indicate RpbA- σ^A contacts whereas colored arrows indicate Fdx contacts to σ^A and RpbA, which includes one shared contact between *Mtb* and *Cdiff* σ^A (red arrow). **b**, Amino acid-sequence alignment of σ^A for diverse representatives of bacteria species. Identical residues are highlighted in yellow. Gaps are indicated by dashed lines. Conserved σ regions are labeled underneath the alignment. Colored boxes indicate contacts to Fdx: blue, unique to *Cdiff*; red, shared between *Cdiff* and *Mtb*. The three letter species code is as follows: Cdf, *Clostridioides difficile*; Bsu, *Bacillus subtilis*; Bun, *Bacteroides uniformis*; Eco, *E. coli*; Mtb, *Mycobacterium tuberculosis*.

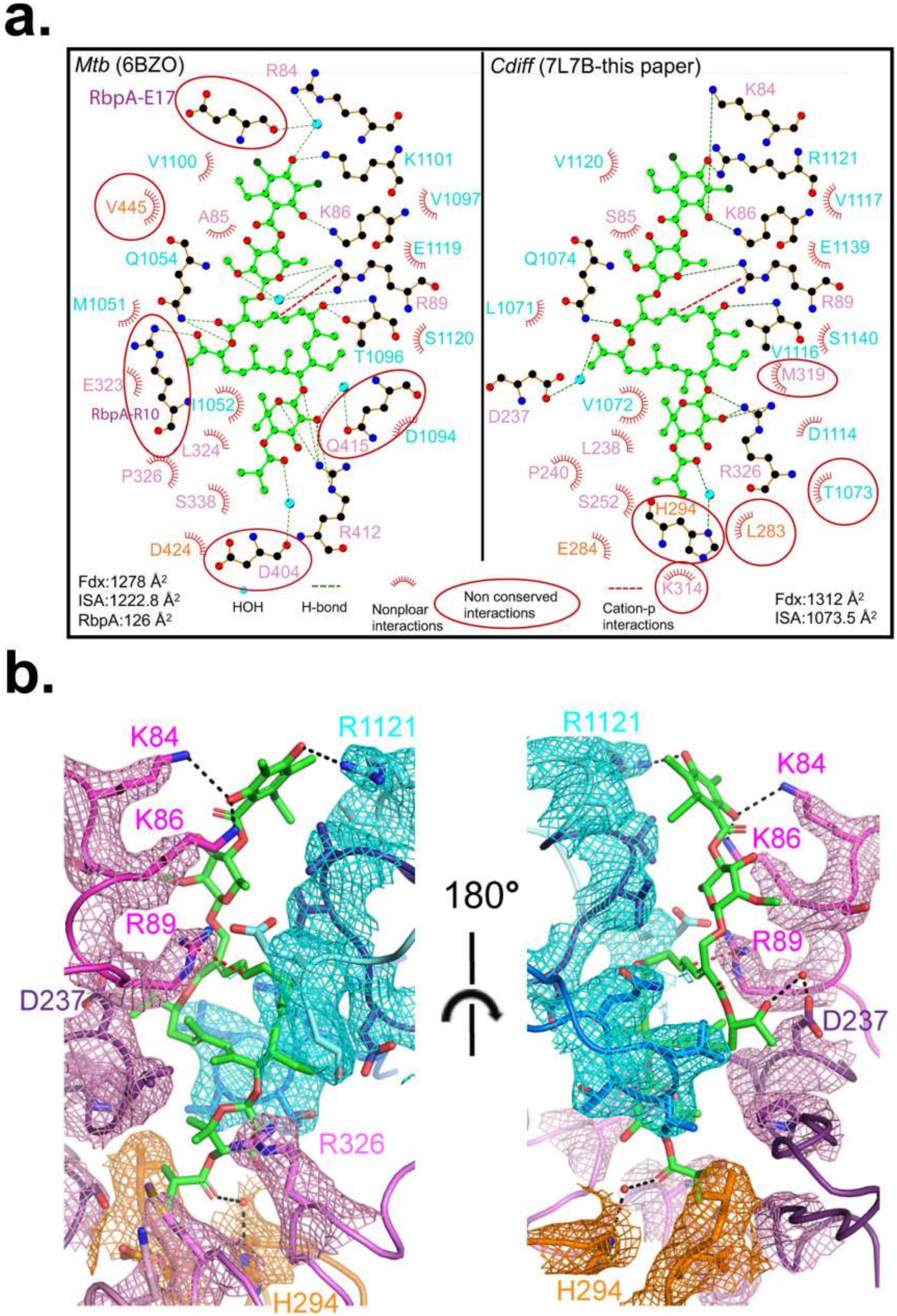

Extended Data Fig. 6 | See next page for caption.

Extended Data Fig. 6 | Fdx binding residues in *Mtb* RbpA-Eσ^A and *Cdiff* Eσ^A. **a**, Ligplot[57] was used to determine contacts between Fdx and *Mtb* RbpA-Eσ^A (left) and *Cdiff* E$\boldsymbol{\sigma}^{\mathbf{A}}$ (right). Cyan sphere, H_2O; green dashed line, hydrogen bond or salt bridge; red arc, van der Waals interactions; red dashed line, cation-π interactions. Note that in ligplot of the *Cdiff* Eσ^A/Fdx interactions, V1143 (discussed in the text as one of the residues when mutated cause Fdx-resistance) did not make the distance cutoff (4.5 Å) as it was located 4.7 Å away from Fdx. The RNAP β, β' and σ^A residues are in cyan, pink, and orange respectively. The two *Mtb* RbpA residues (E17, R10) that interact with Fdx are colored in purple and indicated in the text. The Fdx-interacting residues that do not have corresponding interactions between *Cdiff* and *Mtb* are highlighted in red circles. **b**, The cryo-EM density map of residues interacting with Fdx. Coloring of the residues is consistent with RNAP subunits coloring in Fig. 3, the stick model and cryo-EM densities are color-coded as follows: Pink: β-subunit, cyan: β′- subunit, and orange: σ^A. Water molecules are shown as red spheres. The residues that form hydrogen bonds (black dotted line) with Fdx are labeled.

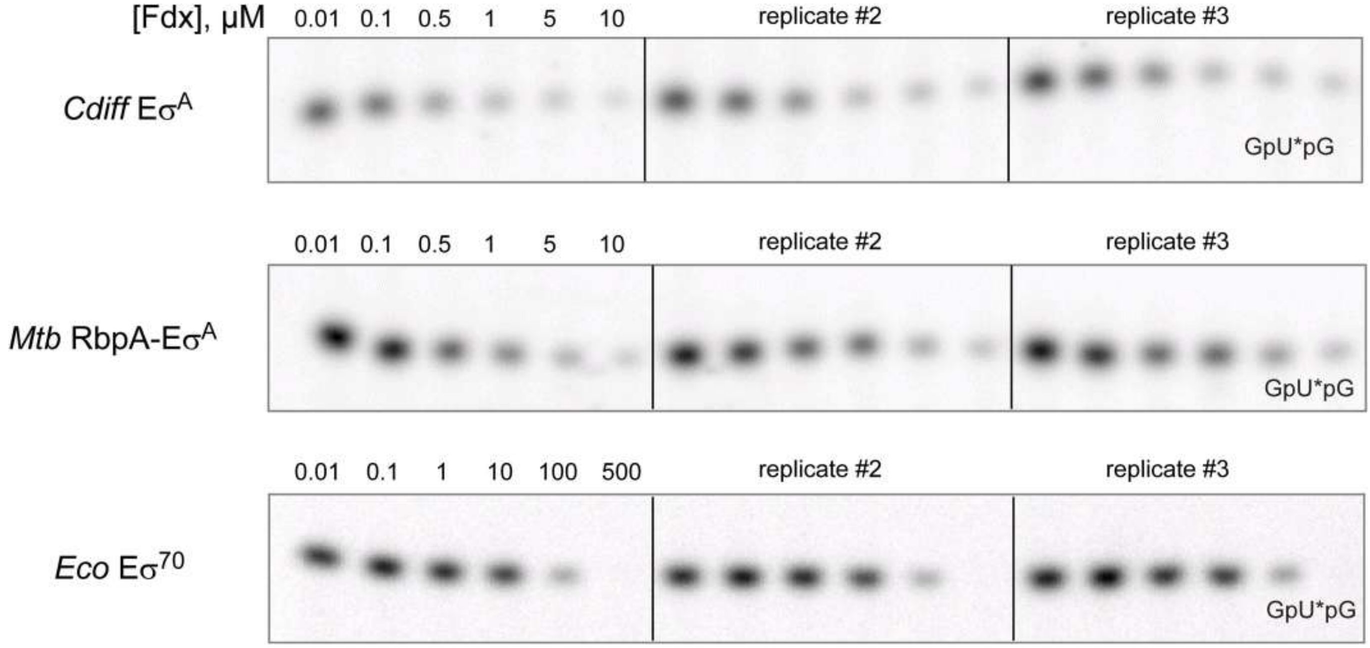

Extended Data Fig. 7 | *In vitro* abortive transcription assays used to determine Fdx IC50 of *Cdiff* and *Mtb* Eσ^A and *Eco* Eσ^{70} related to Fig. 2d. Abortive ^{32}P-RNA products (GpUpG) synthesized on *Cdiff rrnC* promoter were quantified in the presence of increasing concentrations of Fdx. For each Eσ^A (or Eσ^{70}), three independent experiments were performed and analyzed on the same gel.

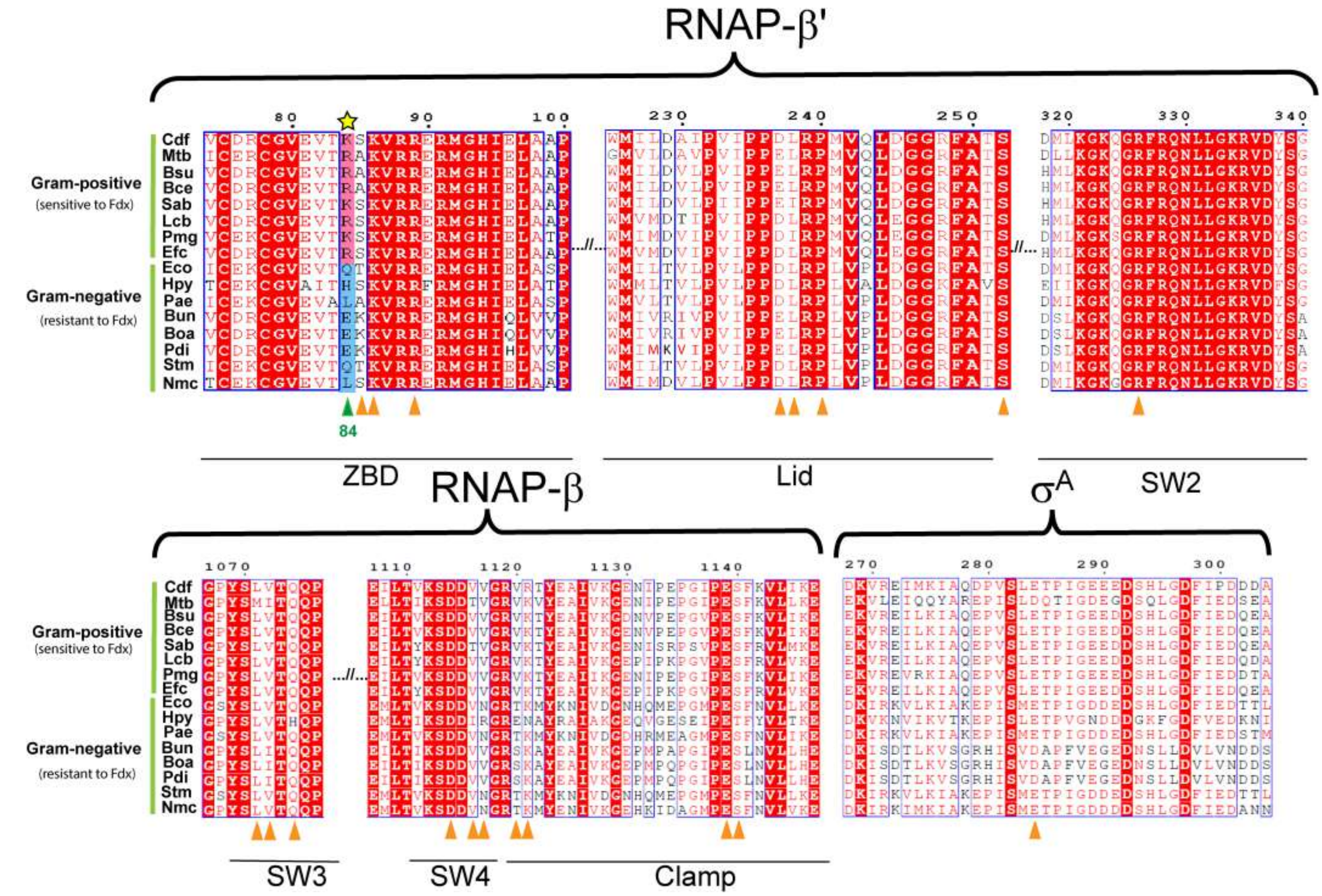

Extended Data Fig. 8 | Comparative sequence alignment of key structural components of RNAPs that interact with Fdx between Fdx-resistant and sensitive bacteria. The Fdx interacting regions are labeled on the top of sequence alignment. Locations of residues contacting Fdx in both *Cdiff* and *Mtb* are labeled by triangles underneath sequences. For gram-positive bacteria that are sensitive to Fdx, the corresponding residue at *Cdiff* β′K84 is either K or R, which is highlighted in pink background. For gram-negative bacteria that are resistant to Fdx, the residue at β′K84 is neutral Q, L, or negative E, which is highlighted in blue background. Conserved residues are shown as white letters on a red background, and similar residues are shown as red letters in blue boxes. Cdf, *Clostridioides difficile*; Mtb, *Mycobacterium tuberculosis*; Bsu, *Bacillus subtilis*; Bce, *Bacillus cereus*, Sab, *Staphylococcus aureus*; Lcb, *Lactobacillus casei*; Pmg, *Peptococcus magna;* Efc, *Enterococcus faecium*; Eco, *Escherichia coli*; Hpy, *Helicobacter pylori*; Pae, *Pseudomonas aeruginosa*; Bun, *Bacteroides uniformis*; Boa, *Bacteroides ovatus;* Pdi, *Parabacteroides distasonis*; Stm, *Salmonella Choleraesuis*; Nmc, *Neisseria meningitidis*.

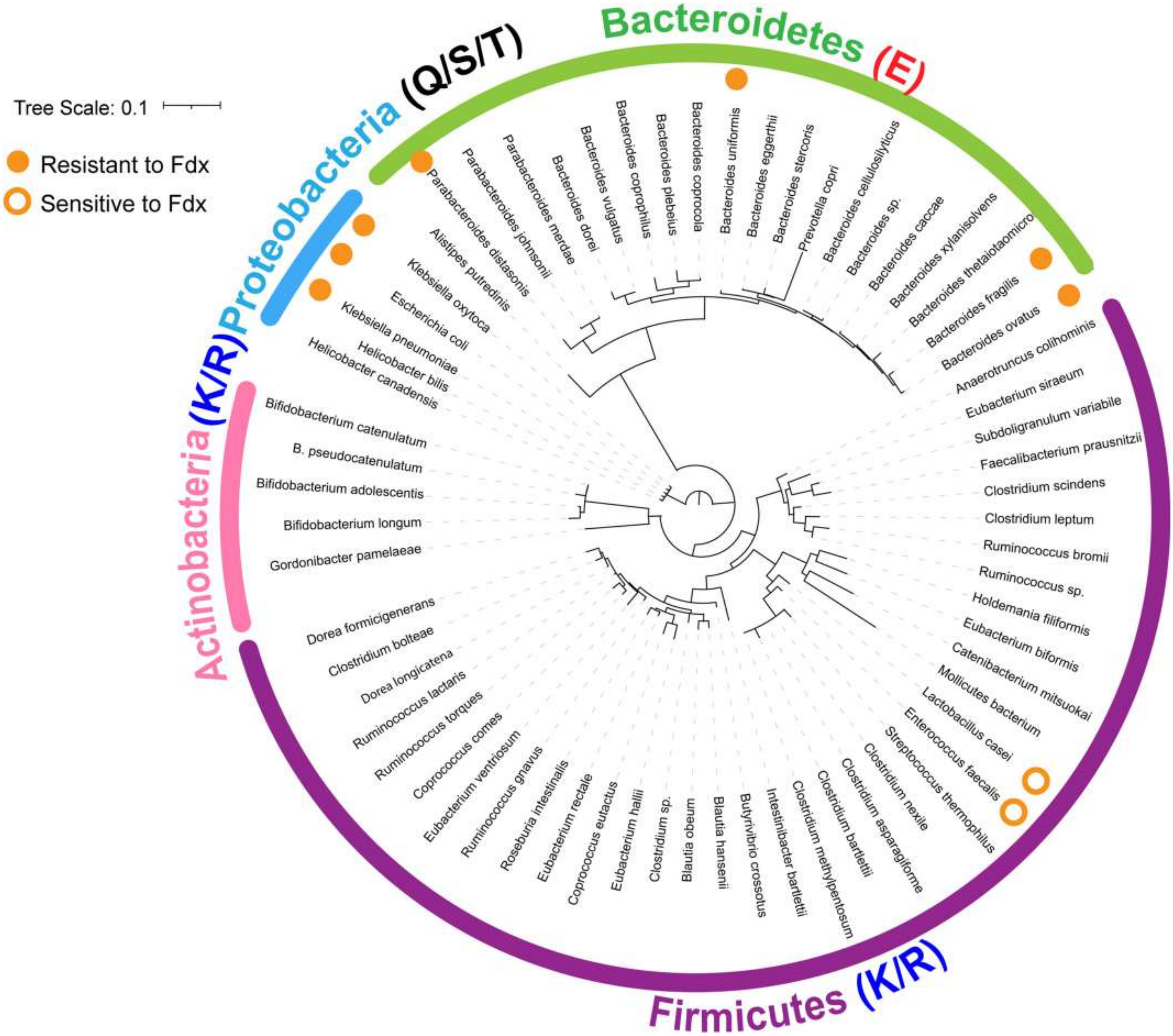

Extended Data Fig. 9 | Phylogenetic tree demonstrating the clade-specific distribution of the identity of the Fdx-sensitizer. The tree displays the identity of the amino acid corresponding to position β′K84 of *Cdiff* in the most common species from human gut microbiota. Bacterial species were largely picked from[28] and[29]. The tree was built from 66 small subunit ribosomal RNA sequences by using RaxML[58] and iTol[59]. Species with experimentally confirmed resistance (MIC > 32 μg/mL) and sensitivity (MIC < 0.125 μg/mL) to Fdx are marked with solid and open orange circle respectively[25]. The amino acid sequence at β′K84 position for corresponding bacteria phyla is denoted by capital letters. The detailed bacterial species are listed in Supplementary Table 4.

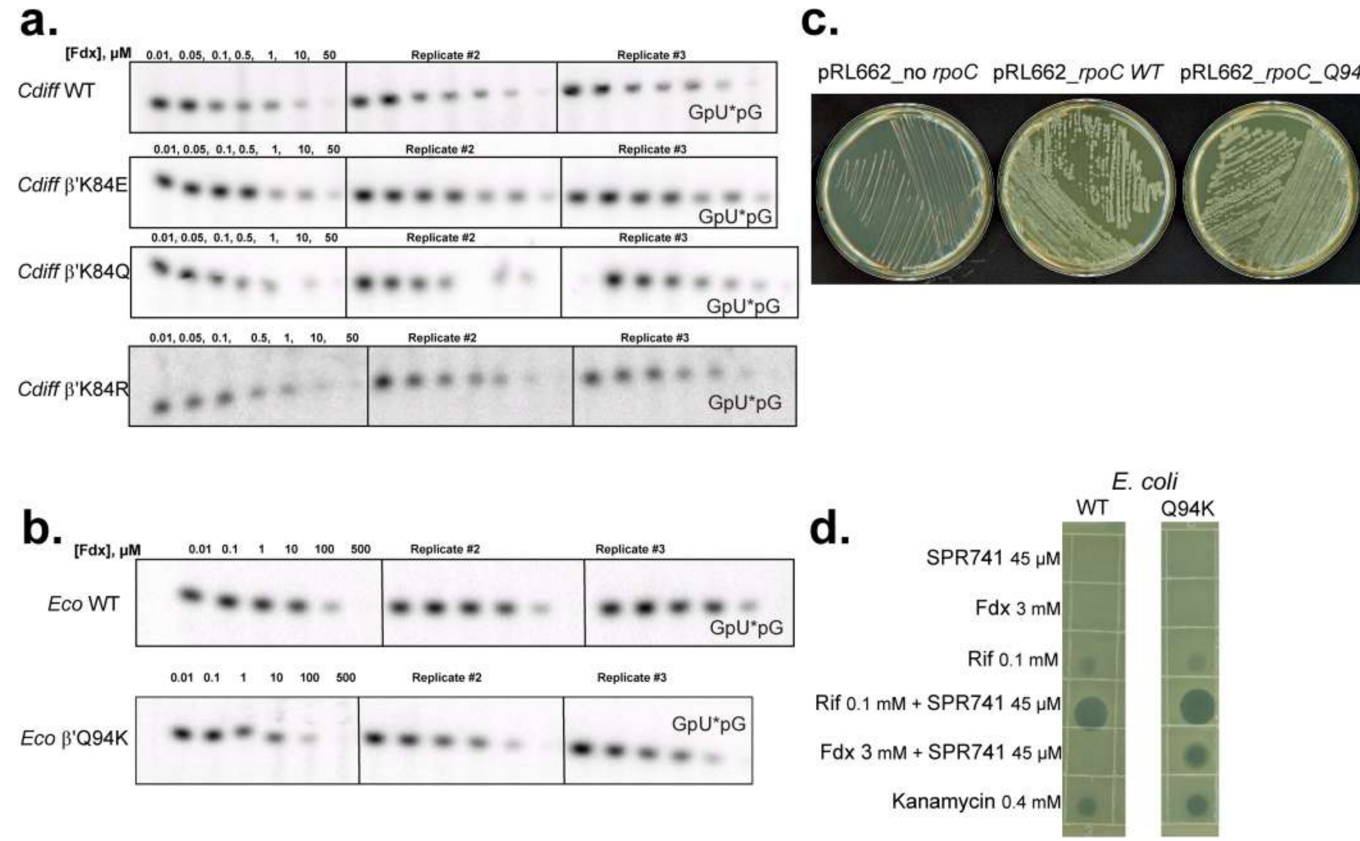

Extended Data Fig. 10 | Fdx inhibition of WT and mutant *Cdiff* and *Eco* RNAPs. a, Transcription assays for *Cdiff* WT, β′K94E and β′K84Q $E\sigma^{A}$s are related to Fig. 4b. The *Cdiff rrnC* promoter (Fig. 2c) was used as a template. **b**, Transcription assays for *Eco* WT and β′Q94K $E\sigma^{70}$s related to Fig. 4c. The same *Cdiff rrnC* promoter was used. For each RNAP, three independent experiments were performed and analyzed on the same gel. **c**, *In vivo* assays on agar plates for *E. coli* WT and Q94K mutant strains. Temperature-sensitive strain RL602 was transformed with control plasmid pRL662 encoding no *rpoC*, WT *rpoC* and mutant *rpoC*-Q94K. Strains were grown overnight at 40 °C. Bacteria containing plasmids expressing *rpoC* WT and Q94K grew well while the empty plasmid does not cell support growth. **d**. Antibiotic inhibition assays using *E. coli rpoC* WT and mutant strains from panel (c). Antibiotics in 3 μL DMSO (Fdx, SPR741, and rifampicin (Rif)) or water (kanamycin (Kan))were pipetted onto overlay soft agar containing the bacteria (see Methods). SPR741 did not inhibit cell growth but increased the potency of Rif and Fdx, suggesting that it increased antibiotic diffusion into the cells. Rif, an antibiotic that targets a region of RNAP distinct from Fdx (± SPR741), and Kan, an antibiotic that targets the ribosome and is not affected by SPR741, equally inhibited the WT and mutant Q94K strains. In contrast, Fdx potently inhibited only the mutant strain, establishing that the Q94E mutation conferred specific sensitivity to Fdx.

nature portfolio

Corresponding author(s): Elizabeth Campbell and Robert Landick

Last updated by author(s): Jan 24, 2022

Reporting Summary

Nature Portfolio wishes to improve the reproducibility of the work that we publish. This form provides structure for consistency and transparency in reporting. For further information on Nature Portfolio policies, see our Editorial Policies and the Editorial Policy Checklist.

Statistics

For all statistical analyses, confirm that the following items are present in the figure legend, table legend, main text, or Methods section.

n/a	Confirmed	
☐	☒	The exact sample size (*n*) for each experimental group/condition, given as a discrete number and unit of measurement
☐	☒	A statement on whether measurements were taken from distinct samples or whether the same sample was measured repeatedly
☒	☐	The statistical test(s) used AND whether they are one- or two-sided *Only common tests should be described solely by name; describe more complex techniques in the Methods section.*
☒	☐	A description of all covariates tested
☒	☐	A description of any assumptions or corrections, such as tests of normality and adjustment for multiple comparisons
☐	☒	A full description of the statistical parameters including central tendency (e.g. means) or other basic estimates (e.g. regression coefficient) AND variation (e.g. standard deviation) or associated estimates of uncertainty (e.g. confidence intervals)
☒	☐	For null hypothesis testing, the test statistic (e.g. *F*, *t*, *r*) with confidence intervals, effect sizes, degrees of freedom and *P* value noted *Give P values as exact values whenever suitable.*
☒	☐	For Bayesian analysis, information on the choice of priors and Markov chain Monte Carlo settings
☒	☐	For hierarchical and complex designs, identification of the appropriate level for tests and full reporting of outcomes
☒	☐	Estimates of effect sizes (e.g. Cohen's *d*, Pearson's *r*), indicating how they were calculated

Our web collection on statistics for biologists contains articles on many of the points above.

Software and code

Policy information about availability of computer code

Data collection	Leginon 3.4
Data analysis	GraphPad Prism 9, ImageQuant 5.2 (GE healthcare), MotionCorr2, CryoSPARC 2, Phenix 1.18.2, Coot 0.8.9.3, Relion 3, LIGPLOT 4.5.3

For manuscripts utilizing custom algorithms or software that are central to the research but not yet described in published literature, software must be made available to editors and reviewers. We strongly encourage code deposition in a community repository (e.g. GitHub). See the Nature Portfolio guidelines for submitting code & software for further information.

Data

Policy information about availability of data

All manuscripts must include a data availability statement. This statement should provide the following information, where applicable:

- Accession codes, unique identifiers, or web links for publicly available datasets
- A description of any restrictions on data availability
- For clinical datasets or third party data, please ensure that the statement adheres to our policy

Cryo-EM maps and atomic models have been deposited in the Electron Microscopy Database (EMDB accession codes 23210) and the Protein Database (PDB accession codes 7L7B).

Field-specific reporting

Please select the one below that is the best fit for your research. If you are not sure, read the appropriate sections before making your selection.

☒ Life sciences ☐ Behavioural & social sciences ☐ Ecological, evolutionary & environmental sciences

For a reference copy of the document with all sections, see nature.com/documents/nr-reporting-summary-flat.pdf

Life sciences study design

All studies must disclose on these points even when the disclosure is negative.

Sample size	We did not perform power analysis for sample size calculation.
Data exclusions	We excluded some particles from our cryo-EM data based on their 2-D projections and 3D reconstruction due to their shape not resembling our complex such as contaminations and/or low-resolution features.
Replication	Experiments were performed 2-3 biological replicates, each with three technical replicates (see figure legends for detail). Biological replicates were performed on different days within 2 weeks.
Randomization	Randomization does not apply to our study as it does not involve clinical data.
Blinding	Blinding does not apply in our study as it does not involve clinical data.

Reporting for specific materials, systems and methods

We require information from authors about some types of materials, experimental systems and methods used in many studies. Here, indicate whether each material, system or method listed is relevant to your study. If you are not sure if a list item applies to your research, read the appropriate section before selecting a response.

Materials & experimental systems

n/a	Involved in the study	
☒	☐	Antibodies
☒	☐	Eukaryotic cell lines
☒	☐	Palaeontology and archaeology
☒	☐	Animals and other organisms
☒	☐	Human research participants
☒	☐	Clinical data
☒	☐	Dual use research of concern

Methods

n/a	Involved in the study	
☒	☐	ChIP-seq
☒	☐	Flow cytometry
☒	☐	MRI-based neuroimaging